

# Ion irradiation of III-V semiconductor surfaces: From self-assembled nanostructures to plasmonic crystals

Cite as: Appl. Phys. Rev. **6**, 041307 (2019); doi: [10.1063/1.5079908](https://doi.org/10.1063/1.5079908)

Submitted: 5 November 2018 · Accepted: 29 August 2019 ·

Published Online: 23 October 2019



[View Online](#)



[Export Citation](#)



[CrossMark](#)

M. Kang<sup>a)</sup> and R. S. Goldman<sup>b)</sup> 

## AFFILIATIONS

Department of Materials Science and Engineering, University of Michigan, Ann Arbor, Michigan 48109, USA

Note: This paper is part of the special topic on Ion Beam Enabled Nanoscale Fabrication, Surface Patterning and Self-Assembly.

<sup>a)</sup>Current address: CREOL, College of Optics and Photonics, University of Central Florida, Orlando, FL 32816, USA.

<sup>b)</sup>Electronic mail: [rsgold@umich.edu](mailto:rsgold@umich.edu)

## ABSTRACT

Ion-irradiation of semiconductor surfaces has emerged as a promising approach to generate a variety of self-organized nanostructures. Furthermore, the combination of focused-ion-irradiation with molecular-beam epitaxy provides unprecedented design and control of surfaces and interfaces of hybrid materials at the atomic level during fabrication. In this review, we describe the directed self-assembly of nanostructure arrays ranging from islands to nanorods to 3-dimensional nanoparticle (NP) arrays. First, we discuss focused-ion-irradiation of III-V surfaces, which leads to preferential sputtering of group V species, followed by the formation of group III-rich metallic nanostructures. For continued irradiation beyond a threshold dose, the nanoparticle (NP) evolution is determined by the sputtering yield and the local ion beam angle of incidence, resulting in arrays of nanoparticles, nanorods, or nanoparticle chains. In addition to describing the formation of close-packed embedded Ga:GaAs nanocomposites using overgrowth of focused-ion-beam fabricated NP arrays, we discuss the surface plasmon resonances of NP arrays as well as the influence of both surface and buried NP arrays on the GaAs photoluminescence efficiency. Finally, we discuss the potential of “plasmonic crystals” for plasmon-enhanced optoelectronics.

Published under license by AIP Publishing. <https://doi.org/10.1063/1.5079908>

## TABLE OF CONTENTS

I. INTRODUCTION .....	1
II. FIB-IRRADIATION-INDUCED SPUTTERING .....	3
A. Sputtering yield trends.....	3
B. Surface nonstoichiometry and threshold ion dose.	3
III. BEYOND THRESHOLD FIB IRRADIATION:	
NANOSTRUCTURE ARRAY FORMATION .....	5
A. Moderate sputtering yield: Ga NPs on GaAs.....	6
B. High sputtering yield: GaSb NRs on GaSb.....	7
C. Low sputtering yield: Ga NCs on GaN .....	8
IV. 3-D NANOCOMPOSITES .....	9
V. OPTICAL PROPERTIES OF PLASMONIC	
NANOCOMPOSITES.....	12
A. Surface plasmon resonances of Ga NP arrays....	12
B. Ga NP plasmon-enhanced GaAs	
photoluminescence .....	12
C. Remaining issues and suggestions .....	13
VI. SUMMARY.....	15

## I. INTRODUCTION

In recent decades, advances in nanofabrication processes have enabled the formation of nanoparticle (NP) arrays with tailored NP geometries and array configurations.<sup>1–12</sup> For example, top-down approaches such as electron-beam lithography (EBL) and nanoimprint lithography (NIL) have been used to fabricate a wide variety of array geometries, with well-controlled NP sizes and spacings.<sup>1</sup> However, EBL- and NIL-based fabrication involves complex multilevel processing, including thin film deposition, lithographic patterning, and chemical etching. Alternatively, hybrid processes that combine top-down and bottom-up approaches have been used to transform surface metallic layers into metallic NP arrays, providing a greater flexibility in NP geometry, often at the expense of the uniformity of NP sizes and spacings.<sup>2–10</sup> Examples include thin film deposition followed by annealing-induced dewetting<sup>2–9</sup> and solution-based NP assembly using linker molecules.<sup>10</sup> Finally, bottom-up approaches such as controlled aggregation of NPs have been achieved via the placement of

drops of NPs in an aqueous solution on prepatterned trenches<sup>11</sup> and/or via encapsulation of NP aggregates in polymeric shells.<sup>12</sup>

In recent years, ion irradiation has emerged as a promising bottom-up approach for self-assembly on a variety of semiconductor surfaces.<sup>13–36</sup> In addition, focused-ion-beam (FIB)-irradiation has been used to induce random distributions of surface nanostructures including nanorods (NRs),<sup>14–17</sup> NPs,<sup>13,18–33</sup> nanoislands,<sup>28</sup> nanoripples,<sup>16,34–36</sup> and nanochains (NCs).<sup>29,30</sup> Furthermore, FIB-irradiation of surface hole arrays has been used to generate arrays of metallic NPs, vertical NRs, and lateral NCs.<sup>23,25,26,29–31,33</sup> On semiconductor surfaces, ion-induced nanostructure formation is often attributed to the segregation of the ion species due to its limited solubility in the target material.<sup>37</sup> For III–V compounds, such as GaAs, a single-phase line compound is expected when the stoichiometry is exactly 1:1, as shown

in the equilibrium phase diagram in Fig. 1(a).<sup>38</sup> For deviations from the 1:1 stoichiometry, the equilibrium phases at room temperature are GaAs plus either Ga or As. Since ion irradiation disrupts the surface stoichiometry, and the sputtering yields of group V elements are typically higher than those of group III elements, ion irradiation often leads to the formation of group III-rich surfaces, as shown in Fig. 1(b).<sup>39–45</sup> Furthermore, sputtering-induced self-assembly, in which ion-irradiation of a flat surface induces spontaneous development of nanoscale morphologies, has emerged as a promising candidate for nanopatterning.<sup>46–49</sup> Since ion implantation is currently used for doping, it would be straightforward to use the same instrumentation for another purpose. Finally, ion sputtering-induced self-assembly is a single-step process; thus, it could be more competitive than multistep approaches involving EBL.<sup>50–53</sup> Both FIB and EBL are serial and maskless

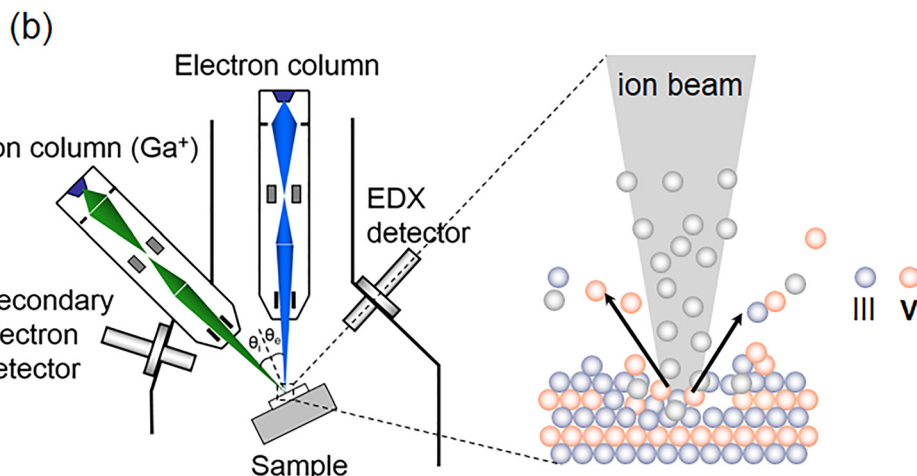
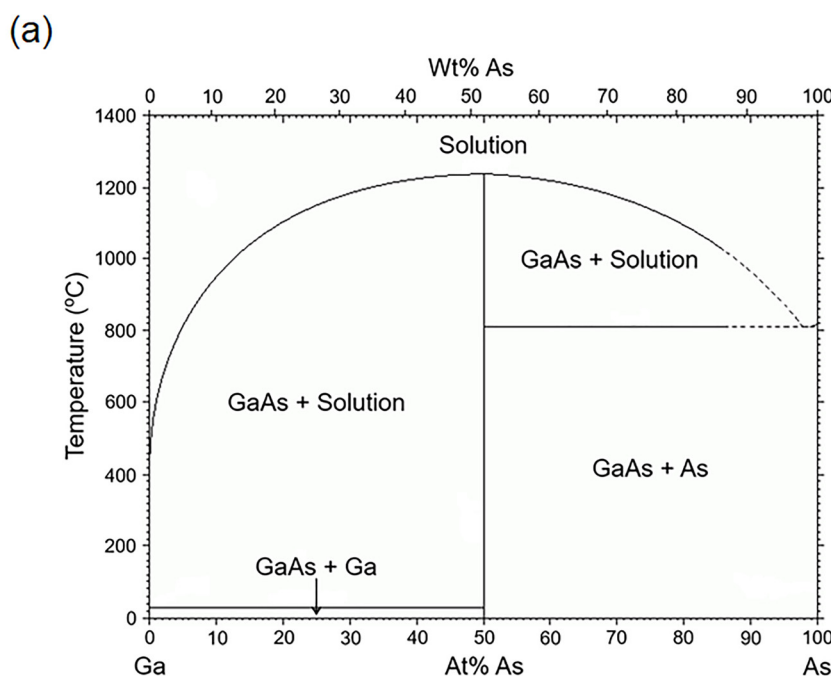


**FIG. 1.** (a) Equilibrium phase diagram of GaAs, a single-phase line compound. At room temperature, deviations from the 1:1 stoichiometry are predicted to lead to the coexistence of GaAs plus either Ga or As. Thus, focused-ion-beam (FIB) irradiation, which induces preferential sputtering of As, is expected to lead to the coexistence of liquid Ga plus solid GaAs. (b) Left: Diagram of NOVA 200 dual beam workstation.  $\theta_i$  ( $\theta_e$ ) is defined as the angle between the incident ion (electron) beam and the sample surface normal represented by the dashed line. For normal-incidence FIB irradiation, the sample is tilted to 52° with respect to the incident electron beam. Right: Illustration of preferential sputtering of group V atoms (red circles) during ion irradiation, leading to a group III (blue circles)-rich surface. Figure 1(a) from H. Okamoto, M. E. Schlesinger, and E. M. Mueller, *ASM Handbook: Alloy Phase Diagrams Volume 3*. Copyright 1992 ASM International. Reproduced with permission from ASM International.

processes; however, the lower mass of electrons in comparison with that of ions limits their applicability to sputtering-induced surface patterning.

In this review, we describe recent progress in the FIB irradiation-directed self-assembly of metallic nanostructure arrays on III-V compound semiconductor surfaces. In Sec. II, we describe semiquantitative calculations of sputtering yield, surface nonstoichiometry, and the resulting threshold ion dose for nanostructure nucleation. In Sec. III, the relationship between the sputtering yield trends and ion-induced nanostructure array formation is discussed in the context of three example Ga-V surfaces: GaAs, GaSb, and GaN. Next, in Sec. IV, we describe the conversion of FIB-patterned surface nanostructures into 3-dimensional (3-D) nanocomposites, with an emphasis on GaAs:Ga nanocomposite fabrication. In Sec. V, we describe a combined computational-experimental approach for tailoring the optical properties of plasmonic nanocomposites (plasmonic crystals), specifically Ga NP plasmon-enhanced photoluminescence efficiencies of GaAs gain media. Finally, we discuss the issues and opportunities offered by plasmonic crystals for enhancing optoelectronic applications.

## II. FIB-IRRADIATION-INDUCED SPUTTERING

In this section, we describe calculations of sputtering yield, surface nonstoichiometry, and the resulting threshold ion dose for nanostructure nucleation. First, we discuss FIB irradiation of III-V surfaces. In particular, we discuss the role of preferential sputtering of group V species on the formation of group III-rich NPs. We also consider the influence of the ion beam angle of incidence on sputtering yield and the resulting impact on the threshold ion dose for nanostructure nucleation.

### A. Sputtering yield trends

During ion irradiation, sputtering of constituent elements is often quantified by the sputtering yield,  $Y$ , defined as the number of sputtered atoms per incident ion. For III-V compounds, the sputtering yield is the sum of the sputtering yields of the group III and group V species, i.e.,  $Y_{\text{III-V}} = Y_{\text{III}} + Y_{\text{V}}$ . Each of  $Y_{\text{III}}$  and  $Y_{\text{V}}$  depend on the mass, valence, and energy of the incident ions as well as the mass, valence, and cohesive energy of the target.<sup>39–45</sup> To calculate sputtering yields of III-V compounds, we assume that the collision between incident ions and target atoms involves a linear collision cascade where the density of mobile target atoms is sufficiently low that atomic collisions may be ignored.<sup>39–41,45</sup> With  $Y_{\text{tot}}$  estimated by Sigmund's sputtering theory,

$$Y_{\text{tot}} = \frac{4.2\alpha S_n}{U_{\text{target}}}, \quad (1)$$

where  $\alpha$  is the correlation factor, which accounts for the partial screening of the nuclear charges of the projectile and target, both of which are not included in the Rutherford cross section;  $S_n$  is the nuclear stopping cross section; and  $U_{\text{target}}$  is the energy needed to separate the constituents of a solid into neutral free atoms at rest, i.e., the cohesive energy.  $\alpha$  and  $S_n$  are expressed as follows:<sup>39–41,45</sup>

$$\alpha = 0.15 \left( 1 + \frac{m_{\text{target}}}{m_{\text{Ga}}} \right)^{0.85}, \quad (2)$$

$$S_n(E_0) = \frac{8.462 \times 10^{-15} Z_{\text{Ga}} Z_{\text{target}} m_{\text{Ga}} S_n(\varepsilon)}{(m_{\text{Ga}} + m_{\text{target}})(Z_{\text{Ga}}^{0.23} + Z_{\text{target}}^{0.23})}, \quad (3)$$

where  $E_0$ ,  $Z_{\text{Ga}}$ ,  $Z_{\text{target}}$ ,  $m_{\text{Ga}}$ ,  $m_{\text{target}}$ , and  $S_n(\varepsilon)$  are the energy of the target atoms during a collision cascade, the atomic numbers of incident  $\text{Ga}^+$

ion and target material, the atomic masses of incident  $\text{Ga}^+$  ion and target material, and the nuclear stopping cross section as a function of the reduced energy,  $\varepsilon$ , respectively.<sup>41</sup>  $\varepsilon$  is a unitless quantity which divides the ion-solid interaction into two regimes where nuclear stopping prevails over electron stopping for  $\varepsilon < 30$  and vice versa for  $\varepsilon > 30$ .<sup>41</sup> In our case, since  $\varepsilon < 30$ , nuclear stopping is dominant over electron stopping, and  $S_n(\varepsilon)$ , an empirical formula which quantifies the nuclear stopping cross section as a function of reduced energy, is expressed as follows:

$$S_n(\varepsilon) = \frac{\ln(1 + 1.1383\varepsilon)}{2(\varepsilon + 0.01321\varepsilon^{0.21226} + 0.19593\varepsilon^{0.5})}, \quad (4)$$

where  $\varepsilon$  is expressed as follows:

$$\varepsilon = \frac{32.53 m_{\text{target}} E_0}{Z_{\text{Ga}} Z_{\text{target}} (m_{\text{Ga}} + m_{\text{target}})(Z_{\text{Ga}}^{0.23} + Z_{\text{target}}^{0.23})}. \quad (5)$$

For binary compounds, we use a law of mixtures to calculate atomic mass ( $m_{\text{target}}$ ), atomic number ( $Z_{\text{target}}$ ), and cohesive energy ( $U_{\text{target}}$ ) of the target.<sup>39</sup>

Figure 2 shows the computed values of  $Y_{\text{tot}}$ ,  $Y_{\text{III}}$ , and  $Y_{\text{V}}$  for several III-V compounds as a function of increasing cohesive energy. For all cases,  $Y_{\text{V}}$  values are consistently greater than those of  $Y_{\text{III}}$ , indicating preferential sputtering of group V elements. As denoted by horizontal dashed lines, we define  $Y_{\text{V}} \leq 2.5$ ,  $2.5 \leq Y_{\text{V}} \leq 4$ , and  $Y_{\text{V}} \geq 4$  to be low, moderate, and high sputtering yield, respectively. Due to the relationship between sputtering yields and milling rates,<sup>40</sup> similar trends are expected for the milling rates of the elements and compounds.

### B. Surface nonstoichiometry and threshold ion dose

To derive an expression for the nonstoichiometry of the group-III rich surface region, we define a projected volume and calculate the nonstoichiometry within that volume, as shown in Fig. 3(a). At the

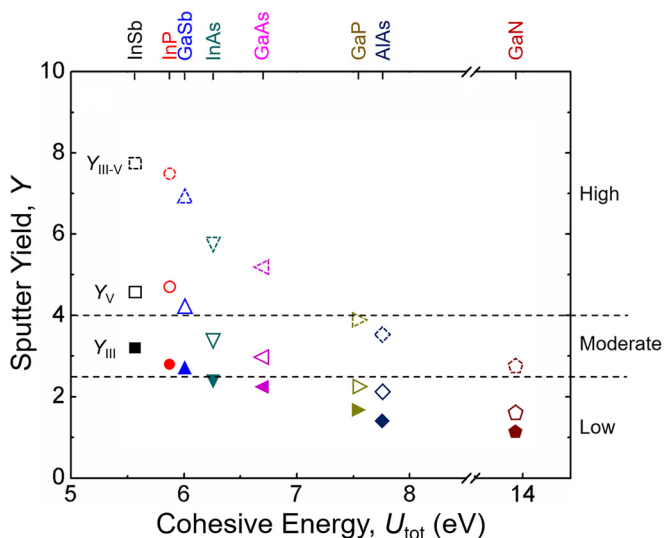


**FIG. 2.** Computed sputtering yields  $Y_{\text{III-V}}$  (dotted),  $Y_{\text{III}}$  (solid), and  $Y_{\text{V}}$  (open) for various III-V compounds as a function of cohesive energy. The horizontal dotted lines divide the value of  $Y_{\text{V}}$  into three sputtering yield ranges: high ( $Y_{\text{V}} \geq 4$ ), moderate ( $2.5 \leq Y_{\text{V}} \leq 4$ ), and low ( $Y_{\text{V}} \leq 2.5$ ).

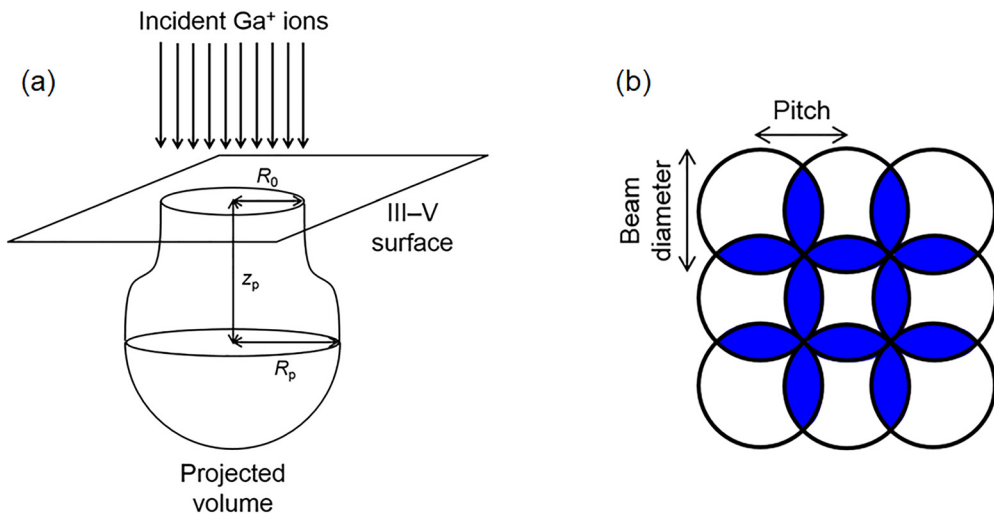


**FIG. 3.** (a) Illustration of projected ion volume near the surface of a III–V compound, showing the ion beam spot radius,  $R_0$ , the longitudinal project ion range,  $z_p$ , and the lateral projected ion range,  $R_p$ . (b) Top-down illustration of raster-scan mode of FIB irradiation, with overlap of sequential beam spots shown in blue.

surface, defined as  $z = 0$ , the normal-incidence ion beam produces a nearly circular cross-sectional area with radius,  $R_0$ . We assume a Gaussian increase in the lateral projected range,  $R(z)$ , from  $R(0) = R_0$  at the surface ( $z = 0$ ) to  $R(z_p) = R_p$  at the end point of the ion trajectory (the longitudinal projected range,  $z = z_p$ ) as follows:<sup>39–41,45</sup>

$$R(z) = R_p e^{-\frac{-\ln \frac{R_p}{R_0}}{z_p}(z-z_p)^2}. \quad (6)$$

The projected volume,  $V_p$ , is then determined by integrating the circular cross-sectional area as a function of the depth from  $z=0$  to  $z_p$ , as shown in Fig. 3(a).

For an initially stoichiometric surface

$$N_{III}(0) = N_V(0) = \frac{V_p \rho}{M_{III} + M_V}, \quad (7)$$

where  $N_{III}(0)$  and  $N_V(0)$  are the initial number of group III and V atoms in the projected volume;  $V_p$  is the projected volume;  $\rho$  is the mass density of the III–V compound; and  $M_{III(V)}$  is the atomic mass of group III (V) elements. The sum of the sputtered group III and V elements is expressed as follows:

$$N_{S,III}(t) + N_{S,V}(t) = (Y_{III} + Y_V) \cdot \frac{dN_{ion}}{dt} \cdot t, \quad (8)$$

where  $dN_{ion}/dt$  is the  $\text{Ga}^+$  ion dose rate, quantified as  $dN_{ion}/dt = I/qA$  ( $I$ =ion beam current,  $q$ =elementary charge, and  $A$ =the cross-sectional area);  $t$  is the irradiation time; and  $Y_{III(V)}$  is the sputtering yield of group III (V) elements. Following ion-irradiation for a time  $t$ , the number of excess group III elements sputtered from the projected volume is expressed as follows:

$$N_{S,V}(t) - N_{S,III}(t) = (Y_V - Y_{III}) \cdot \frac{dN_{ion}}{dt} \cdot t, \quad (9)$$

where  $N_{S,III}(t)$  and  $N_{S,V}(t)$  are the number of group III and V atoms sputtered from the projected volume following ion-irradiation for a

time  $t$ , respectively. Next, we define the surface nonstoichiometry,  $\delta$ , in terms of  $\text{III}_{1+\delta}\text{V}_{1-\delta}$ . Following ion-irradiation for a time  $t$ ,  $\delta$  is given by the ratio of the difference to the sum of group III ( $N_{III}(t)$ ) and group V ( $N_V(t)$ ) elements within  $V_p$  as follows:

$$\delta = \frac{[N_{III}(t) - N_V(t)]}{[N_{III}(t) + N_V(t)]}, \quad (10)$$

where  $N_{III}(t)$  and  $N_V(t)$  are defined as follows:

$$N_{III}(t) = N_{III}(0) - N_{S,III}(t), \quad (11)$$

$$N_V(t) = N_V(0) - N_{S,V}(t). \quad (12)$$

The expression for the nonstoichiometry following ion-irradiation for time  $t$  becomes

$$\delta(t) = \frac{(Y_V - Y_{III}) \cdot \frac{dN_{ion}}{dt} \cdot t}{\left[ 2N_{III}(0) - (Y_{III} + Y_V) \cdot \frac{dN_{ion}}{dt} \cdot t \right]}. \quad (13)$$

Finally, for each ion current, we compute  $\delta$  as a function of ion dose. As will be discussed below, our experiments are performed using raster-scanning, typically with  $\sim 70\%$  beam spot overlap, as illustrated in Fig. 3(b); thus,  $\delta$  is computed in the regions of beam spot overlap.

Figure 4(a) shows the plots of calculated  $\delta$  at an ion dose rate of  $2.2 \times 10^{14}/(\text{cm} \cdot \text{s})$  vs ion dose for InSb, InP, GaSb, InAs, GaAs, GaP, AlAs, and GaN, in the order of increasing cohesive energy. The specific ion dose rate was selected as an example among a range of values used in experimental studies, as shown in Table I. For all cases,  $\delta$  increases monotonically with increasing ion dose. For  $\delta = 1$ , shown as a horizontal bold dashed line in Fig. 2(d), surface nanostructures consisting primarily of group III elements are nucleated; thus, we term this value the “threshold ion dose.” In Fig. 4(a), the threshold ion doses are indicated by vertical dotted lines that intersect the horizontal bold dashed line discussed above. From Fig. 4(a), it is evident that the threshold ion dose increases with increasing III–V cohesive energy.<sup>28</sup>

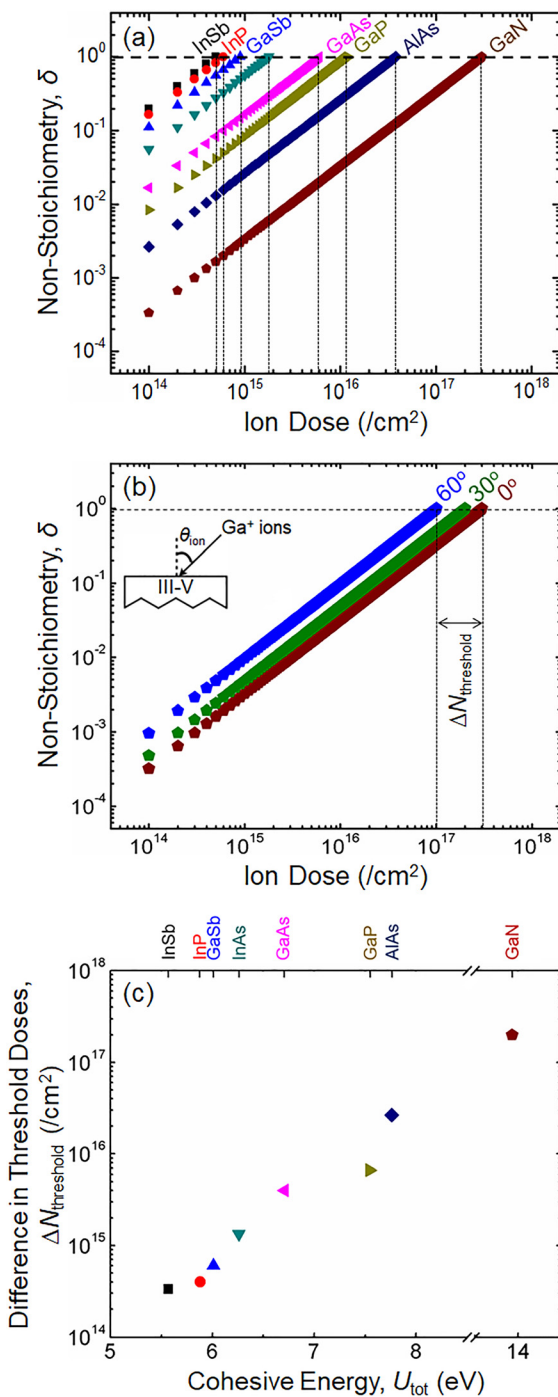


**FIG. 4.** (a) Plots of computed nonstoichiometry,  $\delta$ , vs ion dose, at a dose rate of  $2.2 \times 10^{14}/\text{cm s}$ , for various III-V compounds. For each compound, the ion doses needed to fully deplete group V/segregate group III, i.e., where  $\delta = 1$ , termed the threshold ion dose, are shown as dotted vertical lines. (b)  $\delta$  as a function of ion dose for GaN surfaces at ion incidence angles,  $\theta_{\text{ion}}$ , ranging from  $0^\circ$  to  $60^\circ$  where the difference in threshold ion doses at  $\theta_{\text{ion}} = 0^\circ$  and  $\theta_{\text{ion}} = 60^\circ$  is termed as  $\Delta N_{\text{threshold}}$ . The inset shows the definition of  $\theta_{\text{ion}}$  used in our study. (c)  $\Delta N_{\text{threshold}}$  for a variety of III-V surfaces as a function of cohesive energy.

**TABLE I.** Focused-ion beam parameters used for the formation of nanostructures.

Parameter	Target material		
	GaAs	GaSb	GaN
Ion energy (keV)	5 and 30	30	30
Ion current (pA)	40–60 and 230	50	50
Ion dwell time ( $\mu\text{s}$ )	10	10	100
Ion dose ( $/\text{cm}^2$ )	$3.2 \times 10^{14}$ – $2.0 \times 10^{18}$	$6.0 \times 10^{15}$	$1.0 \times 10^{18}$
Ion dose rate ( $/\text{cm}^2 \text{ s}$ )	$1.8 \times 10^{14}$ – $1.0 \times 10^{15}$	$2.0 \times 10^{14}$	$8.3 \times 10^{14}$
Beam pitch (nm)	6.1 and 12.7	7.1	7.1
Magnification ( $\times$ )	10 000	10 000	20 000
Angle of ion incidence (deg)	0, 26–82	0	0
Irradiation time (s)	1.8–9100	30	1200

Interestingly, the measured ion doses for nucleation of group III-rich surface nanostructures are consistent with these computed threshold ion doses.<sup>28</sup> The sputtering yield is also dependent upon the ion angle of incidence ( $\theta_{\text{ion}}$ ). The depth to which incident ions can penetrate, often termed the ion stopping depth, decreases with increasing  $\theta_{\text{ion}}$ . Therefore, for ion irradiation at higher values of  $\theta_{\text{ion}}$  an increase in the density of near-surface atomic displacements is expected. Accordingly, the sputtering probability and the group III surface composition are expected to increase. In Fig. 4(b), the influence of increasing values of  $\theta_{\text{ion}}$  on the ion-dose dependence of  $\delta$  is shown for GaN surfaces. To quantify the difference in threshold ion dose needed for the surface to reach  $\delta = 1$ , we define a threshold ion dose shift,  $\Delta N_{\text{threshold}}$ . In Fig. 4(c),  $\Delta N_{\text{threshold}}$  is tabulated for a wide range of III-V surfaces, showing that the  $\Delta N_{\text{threshold}}$  value increases with decreasing III-V sputtering yield.

### III. BEYOND THRESHOLD FIB IRRADIATION: NANOSTRUCTURE ARRAY FORMATION

In this section, we describe the impact of irradiation beyond the threshold ion dose, namely, the influence of both surface sputtering yield and  $\theta_{\text{ion}}$  on the formation and evolution of NP arrays. Indeed, the ion dose-dependence of  $\delta$ , shown in Fig. 2(d), suggests that raster-scan FIB irradiation to produce arrays of group III-rich spots would enable the controlled formation of surface nanostructure arrays. For example, as illustrated in Fig. 5(a), FIB patterning up to the threshold ion dose results in group III-rich ( $0 < \delta < 1$ ) hole arrays surrounded by stoichiometric (i.e.,  $\delta = 0$ ) regions, as shown in the inset to Fig. 5(a). Once portions of the irradiated spots have encountered doses within  $\sim 50\%$  of threshold ion dose, subsequent irradiation leads to group III segregation (i.e.,  $\delta = 1$ ) via the nucleation of group III nanostructures. Continued irradiation leads to  $\theta_{\text{ion}}$ -dependent preferential milling which depends upon the sputtering yield of the host surface. In the following, we consider the influence of the group V sputtering yield ( $Y_V = Y_{\text{III-V}} - Y_{\text{III}}$ ) on self-assembled nanostructure array formation in the context of three Ga-V surfaces: GaSb NRs with Ga tips on GaSb surfaces (high sputtering yield:  $Y_V \geq 4$ ), Ga NPs on GaAs surfaces (moderate sputtering yield:  $2.5 \leq Y_V \leq 4$ ), and Ga NCs on GaN surfaces (low sputtering yield:  $Y_V \leq 2.5$ ). Subsequently, in Sec. IV, we will show that FIB-induced 2-D surface nanostructures can be

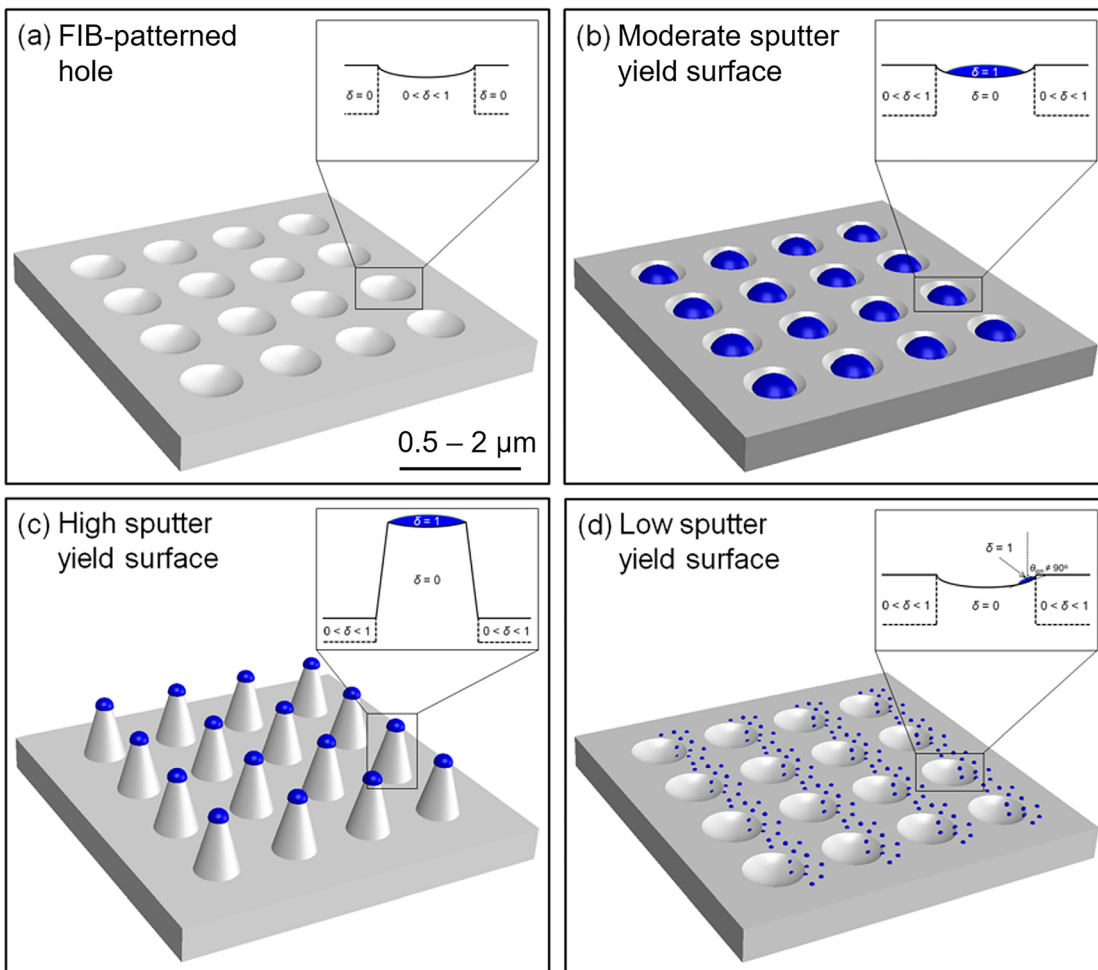


**FIG. 5.** Illustrations of surface morphologies and corresponding local nonstoichiometries,  $\delta$ , for (a) focused-ion-beam (FIB) patterned hole arrays, followed by blanket irradiation of the hole arrays beyond the threshold ion dose for surfaces with (b) moderate ( $2.5 \leq Y_V \leq 4$ ), (c) high ( $Y_V \geq 4$ ), and (d) low ( $Y_V \leq 2.5$ ) sputtering yields. (b) For moderate sputtering yields, blanket irradiation of the hole arrays beyond the threshold ion dose results in group III NP nucleation and growth exclusively within the prepatterned holes. (c) For high sputtering yields, blanket irradiation of the hole arrays beyond the threshold ion dose also leads to the nucleation and growth of group III NPs within the prepatterned holes. These group III NPs subsequently serve as sputtering masks, leading to the preferential sputtering of regions outside the hole, resulting in the formation of arrays of vertical NRs consisting of a III-V body and a group III cap. (d) For low sputtering yields, blanket irradiation of the hole arrays beyond the threshold ion dose, the relatively high threshold ion doses lead to effectively off-normal irradiation with local variations in sputtering yield across the holes. Ga NP nucleation and growth occurs preferentially on hole sidewalls; during continued blanket irradiation, the competition between NP sputtering and group III migration results in the nucleation of small NP at the hole periphery. The scale bar in (a) applies to all cases.

seamlessly transformed into 3-D nanocomposites via molecular beam epitaxy (MBE) overgrowth.

#### A. Moderate sputtering yield: Ga NPs on GaAs

First, we discuss “beyond threshold dose” nanostructure array formation on surfaces with moderate values of sputtering yields,  $2.5 \leq Y_V \leq 4$ , such as GaAs and InP. Following FIB patterning of hole arrays up to the threshold ion dose, the entire region is “blanket” FIB irradiated, until the group III segregation dose (i.e.,  $\delta = 1$ ) is reached within the hole arrays, as shown in Fig. 5(b). Thus, group III nanostructures are nucleated, while the regions beneath the NPs remain

stoichiometric ( $\delta = 0$ ), and the regions between NPs become nonstoichiometric ( $0 < \delta < 1$ ), as shown in the inset to Fig. 5(b). Finally, for the highest ion doses, the regions between the prepatterned holes become nonstoichiometric, resulting in NP nucleation in regions outside the prepatterned holes.<sup>33</sup>

Several example Scanning electron microscope (SEM) images of Ga NP arrays on GaAs surfaces are shown in Fig. 6. These images reveal independent control over the NP diameters (ranging from 60 nm to 340 nm) and inter-NP spacings (ranging from 400 nm to 1500 nm). Typically, the NP diameters are less than or equal to the hole diameters while the NP arrays spacings reflect the hole spacings. In earlier studies, we showed that the NPs within the GaAs surface

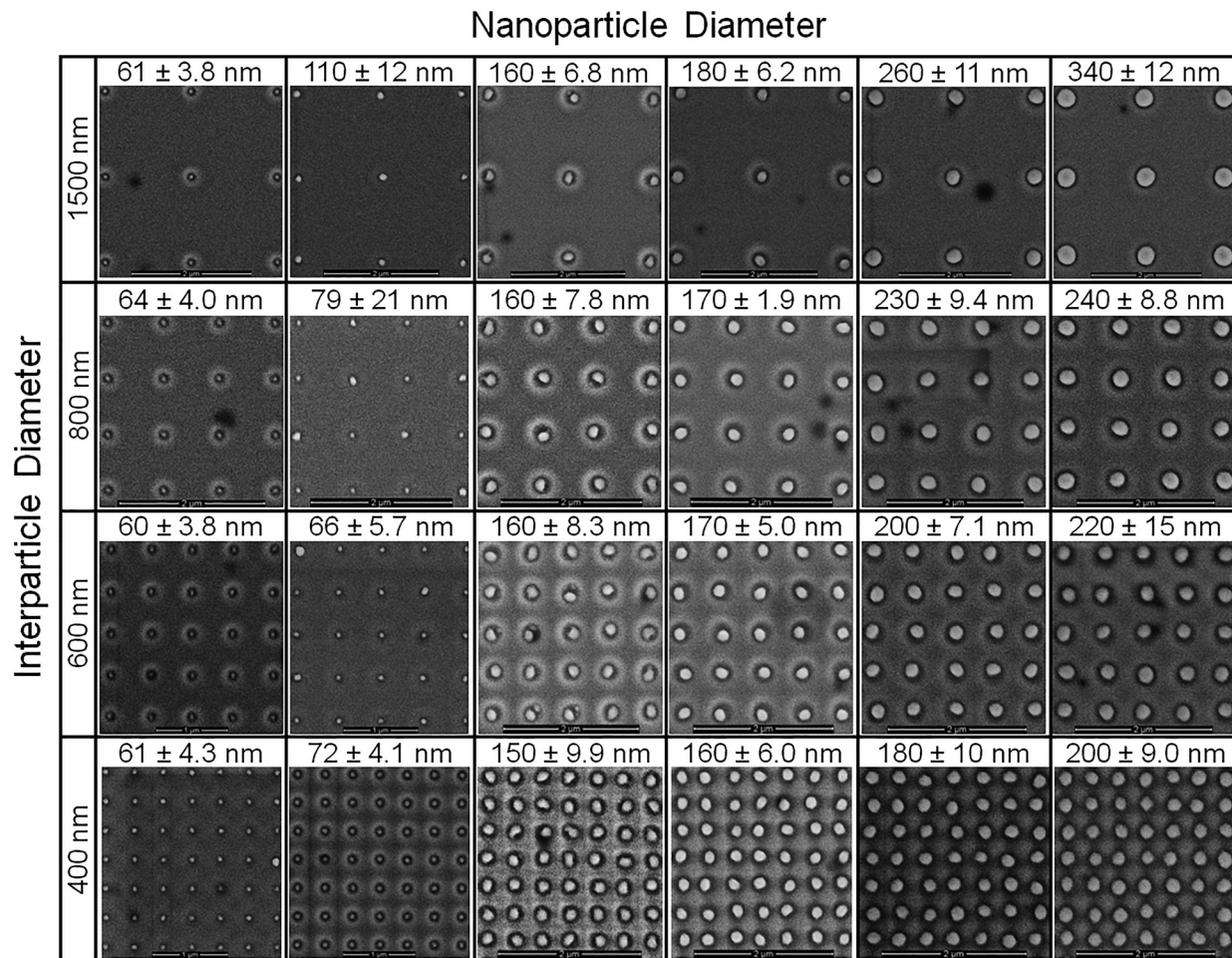


**FIG. 6.** Matrix of Ga nanoparticle (NP) arrays induced on GaAs surfaces by tuning the diameters and separations of the focused-ion-beam (FIB)-fabricated hole arrays. As the hole diameters are varied from 80 nm to 360 nm, the resulting NP diameters range from 60 nm to 340 nm. As the hole separations are varied from 150 nm to 400 nm, the resulting NP spacings range from 400 nm to 1500 nm. Typically, the NP diameters of individual NPs are smaller than the hole diameters, while the NP spacings match the hole spacings. The scale bar in the first panel applies to all cases.

arrays consist primarily of amorphous Ga.<sup>28</sup> For ion doses in the range of  $2.3 \times 10^{16}$  to  $9.0 \times 10^{16}/\text{cm}^2$ , NPs nucleate and grow exclusively in the prepatterned holes.

For ion doses  $< 10^{17}/\text{cm}^2$ , NPs nucleate and grow exclusively in the prepatterned hole arrays, with corner NPs larger than those of side and inner NPs. To consider the relative roles of bulk and surface diffusion on NP array evolution, a series of  $5 \times 5$  NP arrays, shown in Figs. 7(a)–7(d),<sup>33</sup> were prepared. For each NP, the height ( $h$ ) and diameter ( $d$ ) were determined using atomic-force microscopy. The resulting aspect ratios,  $h/d$ , vs ion dose are plotted in Fig. 7(e) for the corner, side, and interior NPs (with two, three, and four nearest-neighbor NPs) that are designated by black, red, and blue symbols. For all NP locations,  $h/d$  increases monotonically with ion dose to a saturation value. Thus, bulk Ga diffusion toward the hole edge leads to vertical Ga NP growth, leading to the increase in  $h/d$ . Beyond the saturation dose,  $h/d$  decreases monotonically, with the lowest aspect ratio values for the corner NPs. At this point, Ga surface diffusion to

the NPs leads to lateral NP growth, leading to the decrease in  $h/d$ . Furthermore, as illustrated in the top left inset to Fig. 7(e), since the Ga NPs with fewer nearest neighbors are able to capture more Ga adatoms, the Ga surface diffusion-induced lateral NP growth is fastest for the corner NPs, leading to the lowest value of  $h/d$ .

## B. High sputtering yield: GaSb NRs on GaSb

We now consider beyond threshold dose nanostructure array formation for III–V compounds with high values of  $Y_V \geq 4$ , such as GaSb and InSb, as shown in Fig. 5(c). Following FIB patterning of hole arrays up to the threshold ion dose, the entire region is blanket FIB irradiated. In this case, due to relatively low threshold ion doses for group III segregation, the group III NPs provide a sputtering mask, while the surrounding stoichiometric III–V regions are milled away.<sup>15,16</sup> Therefore, as shown in Fig. 5(c), arrays of vertical nanorods (NRs) with sloped sidewalls are formed. Each NR consists of a

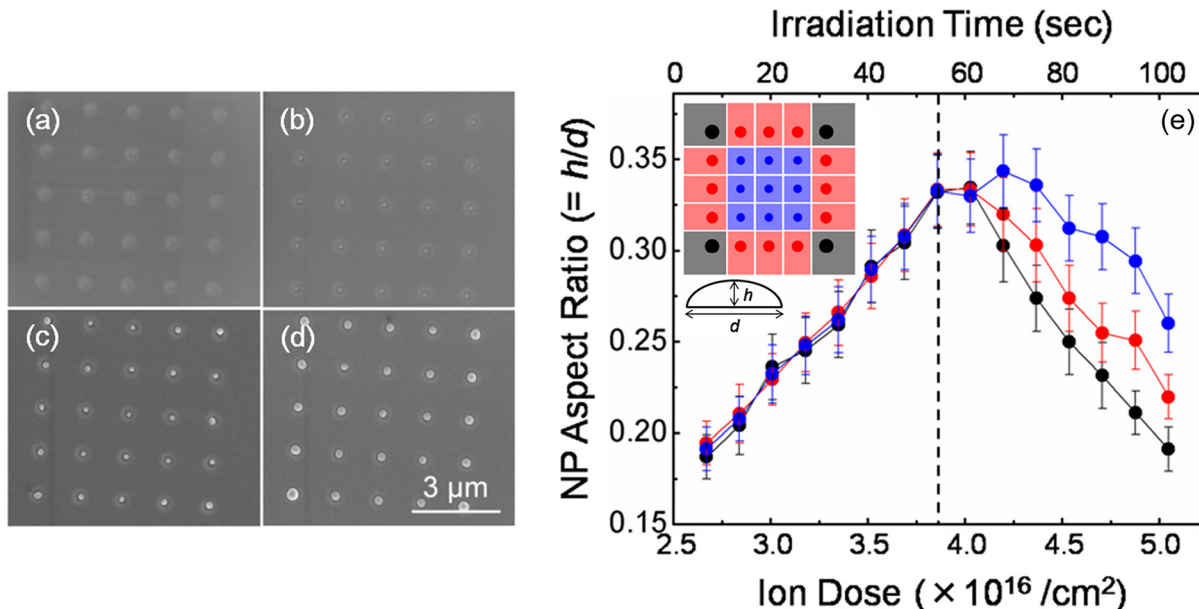


**FIG. 7.** Top-view SEM images of FIB-induced Ga NP arrays for various ion doses: (a)  $2.7 \times 10^{16}/\text{cm}^2$ , (b)  $3.4 \times 10^{16}/\text{cm}^2$ , (c)  $4.1 \times 10^{16}/\text{cm}^2$ , and (d)  $4.8 \times 10^{16}/\text{cm}^2$ . Ga NP diameters increase with ion dose, and the largest Ga NPs exist on corners of arrays, followed by those on sides, and finally the smallest Ga NPs are found on interiors. (e) Plots of aspect ratios of Ga NPs vs ion dose/irradiation time. The inset shows a schematic of the “corner,” “side,” and “interior” Ga NPs within a  $5 \times 5$  array. The NP aspect ratios, defined as  $h/d$ , where  $h$  and  $d$  are the height and diameter of NPs, respectively, increase monotonically with dose to a saturation value which is represented by the vertical dotted line, independent of NP location within the array. Beyond the saturation dose, the NP aspect ratio decreases monotonically, with the lowest aspect ratios for the corner NPs. Figures 7(a)–7(e) reproduced with permission from Appl. Phys. Lett. **104**, 182102 (2014). Copyright 2014 AIP Publishing.

stoichiometric ( $\delta = 0$ ) body with a segregated ( $\delta = 1$ ) cap. The NRs form in the hole arrays, while the regions between the NRs remain nonstoichiometric ( $0 < \delta < 1$ ). If the sputtered group III atoms are also redeposited during the process, the group III caps would remain intact, and the NR sidewalls would be sloped, as shown in Fig. 3(c).

Example SEM and transmission electron microscopy (TEM) images of vertical NRs within hole arrays on GaSb surfaces are shown in Fig. 6. Figure 8 presents the SEM images of (a) an array of vertical NRs, along with (b) a close-up view of an individual NR. Within each array,  $400 \pm 25$  nm length NRs, with sloped sidewalls and  $55 \pm 5$  nm caps, are observed. Redeposition of sputtered atoms may provide seeds for additional NP growth, as has been reported for ion irradiated Au NP arrays.<sup>54</sup> This redeposition effect is expected to be pronounced on surfaces with high sputtering yields. Indeed, in our case, nanoscale features are randomly distributed outside the prepatterned holes containing vertical nanorods on GaSb surfaces, as shown in Fig. 8(b). High resolution views of an individual NR are shown in Figs. 8(c), 8(e), and 8(f), along with a corresponding SAED pattern in Fig. 8(d). In Fig. 8(c), the bright field (BF) TEM image of the NR illustrates the shape of the NR body and NR cap. The SAED pattern in Fig. 8(d) consists of diffuse rings corresponding to amorphous Ga and spotty rings corresponding to the {111}, {220}, {311}, {400} and {331} planes of zinc blende GaSb. The BF high-resolution TEM (HRTEM) images in Figs. 8(c) and 8(d), collected from the NR cap and NR body, reveal that the cap is primarily amorphous while the body contains randomly oriented nanocrystals with a lattice spacing of  $6.0958 \text{ \AA}$ , consistent with those reported for zinc blende GaSb. Figures 8(e)–8(h) show a DF TEM image in STEM mode, along with the corresponding XEDS

maps where green and red denote Ga and Sb, respectively. The XEDS maps reveal a nearly pure Ga cap and a mixture of Ga and Sb in the body. The presence of amorphous Ga caps and polycrystalline GaSb bodies, shown in Figs. 8(b)–8(d), suggests that the NR formation is due to a Ga cap-induced reduction in the local sputtering yield in the region beneath the Ga cap. In addition, as shown in Fig. 6(b), the diameter of the cap is much smaller than that of the lower part of the body, suggesting a cap-induced self-shielding mechanism, possibly assisted by Ga and Sb redeposition on the sidewall of the body. Similar results were obtained for surface nanostructures on ion-irradiated InSb surfaces.<sup>14–16</sup>

### C. Low sputtering yield: Ga NCs on GaN

We now consider beyond threshold dose nanostructure array formation for III–V compounds with low values of  $Y_V \leq 2.5$ , such as GaN, as shown in Fig. 5(d). Following FIB patterning of hole arrays up to the threshold ion dose, the entire region is blanket FIB irradiated. In this case, due to the relatively high values of threshold ion doses, as shown in Fig. 4(a), the  $\theta_{\text{ion}}$ -dependence of the sputtering yield plays a significant role. Since the group III-rich holes are semispheroidal-shaped,<sup>29</sup> irradiation is effectively off-normal, leading to a variation in sputtering yield across the hole, with the highest values at the hole periphery.<sup>27,29</sup> For a sloped sidewall (such as for  $60^\circ$  off-normal irradiation) on the GaN surface, as shown in Figs. 4(b) and 4(c), the threshold ion dose is substantially reduced:  $\Delta N_{\text{threshold}} > 10^{17}/\text{cm}^2$ . Thus, on the hole sidewalls, Ga segregation leading to Ga NP formation occurs at relatively low ion doses, essentially suppressing the subsequent

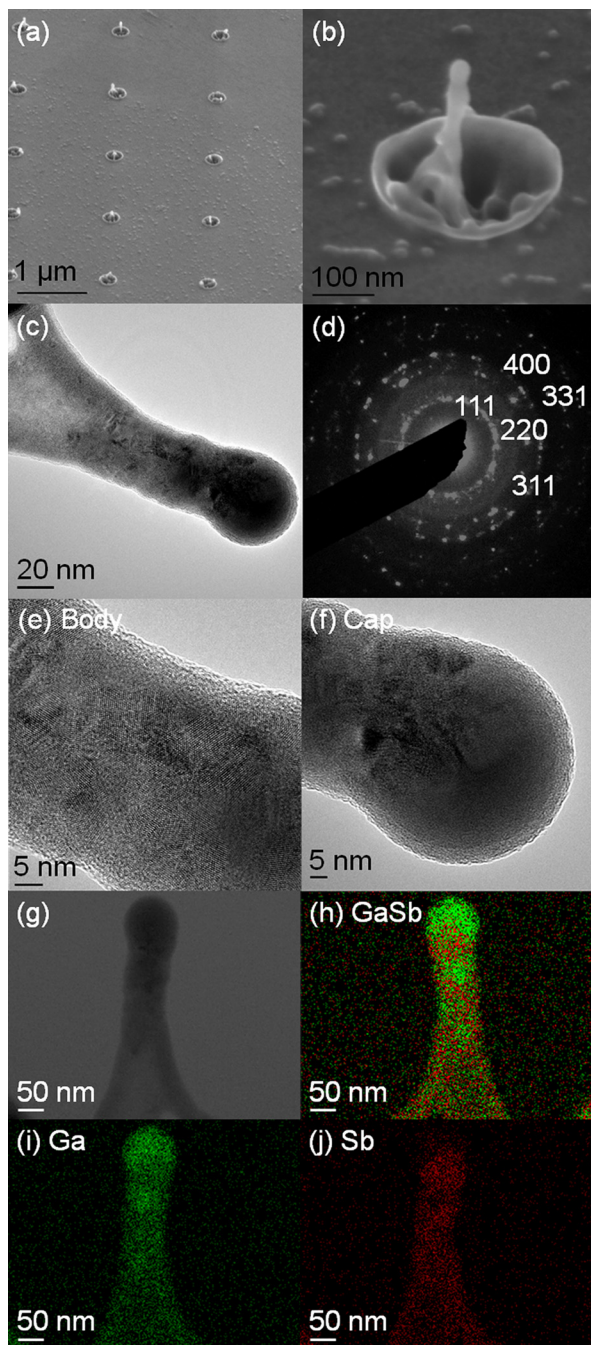


**FIG. 8.** Scanning electron microscope (SEM) images of (a) nanorod (NR) array, along with (b) a close-up view of an individual NR revealing its body and cap. (c) Bright-field (BF) transmission electron microscope (TEM) image and (d) corresponding selected-area electron diffraction (SAED) pattern revealing diffuse rings corresponding to amorphous Ga and spotty rings corresponding to the  $\{111\}$ ,  $\{220\}$ ,  $\{311\}$ ,  $\{400\}$ , and  $\{331\}$  planes of zinc blende GaSb. BF high-resolution TEM images of (e) the NR body and (f) cap suggest that the body consists of zinc blende GaSb ( $d = 6.0958 \text{ \AA}$ ), with an amorphous cap. Dark-field (DF) scanning TEM image (g) and corresponding x-ray energy dispersive spectroscopy (XEDS) maps (h)–(j) reveal both Ga (green) and Sb (red) in the body, with the cap consisting primarily of Ga (green).

nucleation of NPs at the hole centers, as shown schematically in Fig. 5(d). Meanwhile, during the beyond-threshold FIB irradiation process, incident ions also sputter the nanostructures. Thus, the NP sizes are determined by a competition between NP sputtering and migration of group III elements from surrounding group III-rich regions. Since the contribution of sputtering increases with increasing  $\theta_{\text{ion}}$ , the Ga NP size typically decreases with increasing  $\theta_{\text{ion}}$ . For Ga-rich hole arrays with an interhole spacing less than 400 nm, the small Ga NPs at the sidewalls of neighboring holes together form one-dimensional Ga NC arrays, as shown in Fig. 5(d).<sup>29</sup> The critical interhole spacing of 400 nm is likely related to ion irradiation-enhanced Ga surface diffusivity,<sup>33</sup> and further work is needed to identify the underlying mechanism.

Several example SEM images of lateral NC arrays on GaN surfaces are shown in Fig. 9. The SEM images in Figs. 9(a) and 9(b) were collected at viewing angles (i.e., secondary electron detector angles) of  $0^\circ$ , while those in Figs. 9(c) and 9(d) were collected at  $52^\circ$ . The NCs consist of Ga NPs with diameters ranging from 10 nm to 20 nm. It is important to note that Ga NPs are primarily located on the sloped sidewalls of the holes and that the small interhole spacing allows the group of Ga NPs in neighboring holes to form continuous ensembles, leading to one dimensional NC arrays. In an earlier study, we explored the formation of Ga NC arrays at holes with a variety of depths.<sup>29</sup> As the hole depth increases, the fraction of surface area where ion irradiation is off-normal increases; therefore, the nucleation of small NPs at the hole periphery is preferred. The formation of nanochain arrays exclusively on one side of prepatterned holes in Fig. 5(d) and Fig. 9 is likely associated with the ion beam raster scan mode. As the ion beam is immediately scanned over one side of the prepatterned holes in their first row, atoms sputtered from outside the holes are redeposited on nearby regions within the holes. Subsequently, the redeposited regions within the holes would require a higher ion dose for nanochain formation. This process is repeated as the ion beam is scanned over the next row of holes. Therefore, for each row of prepatterned holes, nanochains form at the hole peripheries that first encounter the scanning ion beam. Similar to Ga NP arrays on GaAs surfaces, the diameter of NCs and interchain spacing can be separately controlled by defining the diameter of prepatterned holes and interhole spacing, respectively.

#### IV. 3-D NANOCOMPOSITES

A long-term goal in plasmonics is to selectively place NPs at buried interfaces to improve emission and/or absorption efficiency, while providing flexibility in device design. As described in Sec. I, 3-D device fabrication typically involves multistep processes such as electron beam evaporation and EBL, typically limited to the front or back surface of a device structure. Here, we describe a successful strategy for overgrowth of FIB-fabricated NP arrays, resulting in the formation of close-packed embedded plasmonic Ga:GaAs nanocomposites, i.e., “plasmonic crystals”.<sup>55</sup> An overview of our fabrication process is shown in Fig. 10. In the first step, 2-D Ga NP arrays are fabricated via  $\text{Ga}^+$  FIB-irradiation on III-V compound semiconductor surfaces such as GaAs.<sup>55</sup> The specimens are subsequently transferred into the MBE chamber, typically within 30 min of removal from the FIB chamber to minimize surface oxidation. Following bakeout and preheating processes, the specimens are exposed to simultaneous fluxes of Ga and As with growth rates and V/III beam-equivalent pressure ratios to control the thickness, stoichiometry, and crystallinity of overgrown layers, as shown in Table II. Before, during, and after each overgrowth, the

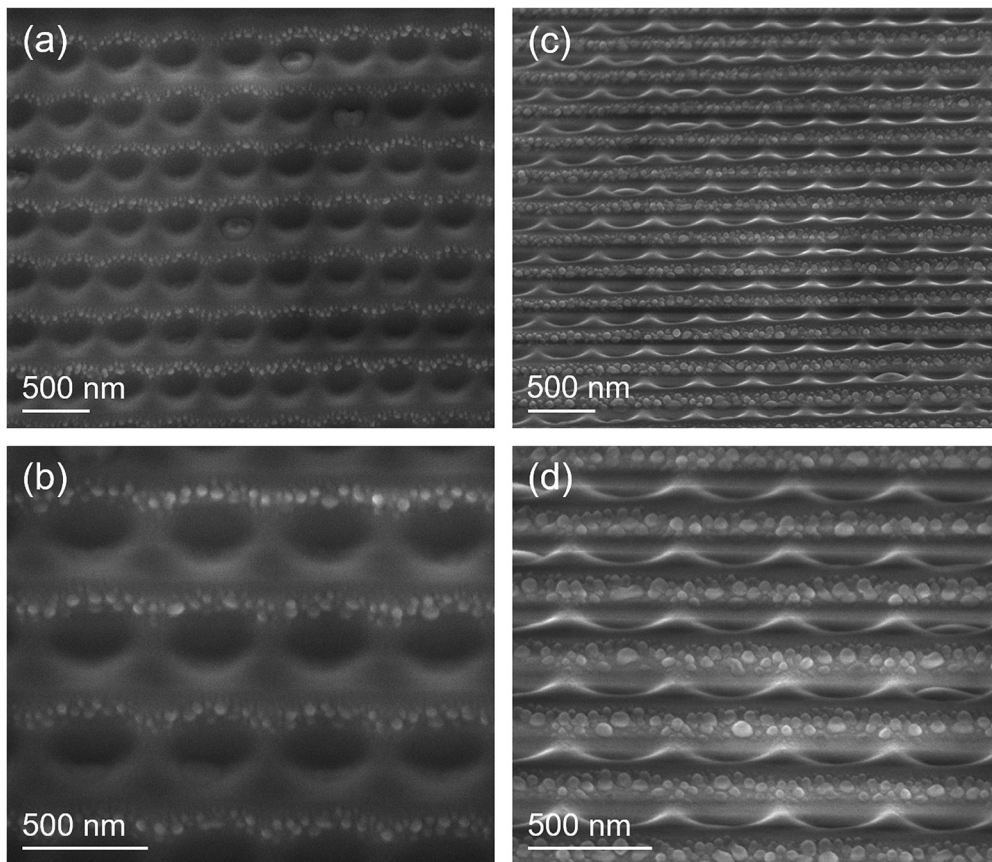


**FIG. 9.** Scanning-electron microscope (SEM) images of lateral nanochain (NC) arrays on GaN surfaces, collected with secondary electron detector angles of (a), (b)  $0^\circ$  and (c), (d)  $52^\circ$ . It is apparent that the 10–20 nm-sized Ga NPs are primarily located on the sloped sidewalls of the prepattered holes. The small interhole spacing allows the group of small and close-packed Ga NPs in neighboring prepattered holes to form continuous ensembles, leading to one dimensional Ga NC arrays with controllable NC diameter and interchain spacing.

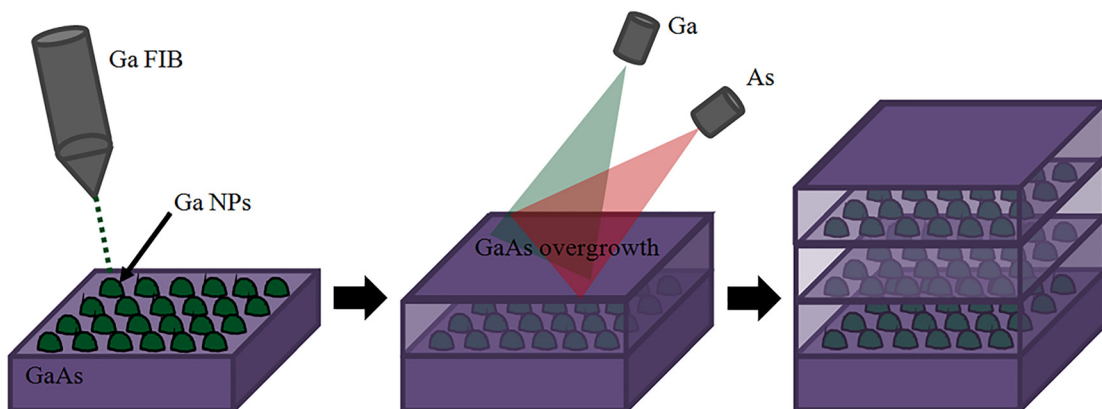


**FIG. 10.** (a) Off-normal  $\text{Ga}^+$  focused-ion-beam (FIB) irradiation is performed in selected  $20 \times 20 \mu\text{m}^2$  regions of GaAs samples. The FIB irradiation induces preferential sputtering of As atoms, leaving behind Ga-rich GaAs surfaces, from which Ga NP arrays are nucleated. Following transfer into the MBE chamber, GaAs layers of various thicknesses are grown atop the entire sample surface.

**TABLE II.** Molecular-beam epitaxy parameters used for the overgrowth of GaAs layers.

Parameter	Value
Load-lock bakeout temperature (°C)	150
Load-lock bakeout time (h)	8
Preheating temperature (°C)	300
Preheating time (min)	10
As <sub>2</sub> flux during heating (Torr)	$5.4 \times 10^{-6}$
Growth temperature (°C)	300
Growth rate ( $\mu\text{m}/\text{h}$ )	1
V/III beam-equivalent pressure ratio during growth	12

surface crystallinity is monitored in real-time using reflection high energy electron diffraction (RHEED). This FIB-assisted MBE approach is likely to enable the realization of a wide range of metal-semiconductor plasmonic crystals.

Figures 11(a)–11(c) show representative atomic force microscopy (AFM) images of surfaces at each step of the FIB-MBE process for fabrication of plasmonic crystals.<sup>55</sup> Specifically, Fig. 11(a) shows a pristine, featureless GaAs surface, without Ga NPs. Its corresponding fast Fourier transform (FFT), shown as an inset to Fig. 11(a), is nearly featureless, consistent with the absence of ordered surface features. Figure 11(b) shows an AFM image of FIB-induced Ga NP arrays on a GaAs surface prior to MBE overgrowth. The Ga NP arrays consist of an average NP diameter of  $40 \pm 6 \text{ nm}$  and an average interparticle spacing of  $72 \pm 9 \text{ nm}$ . In the corresponding FFT shown in the inset to Fig. 11(b), a hexagonal spot pattern with a split center spot, indicating the existence of a sixfold symmetry with a superimposed twofold symmetry, is observed, consistent with the AFM image of elongated hexagonal arrays of NPs. Following 50 nm-thick overgrowth of the NP arrays, similar elongated hexagonal arrays are observed with corresponding FFT consisting of hexagonal patterns with a split center spot, as shown in Fig. 11(c).

To assess the crystalline quality and microstructure of the MBE-overgrown Ga:GaAs nanocomposites, both *in situ* RHEED patterns

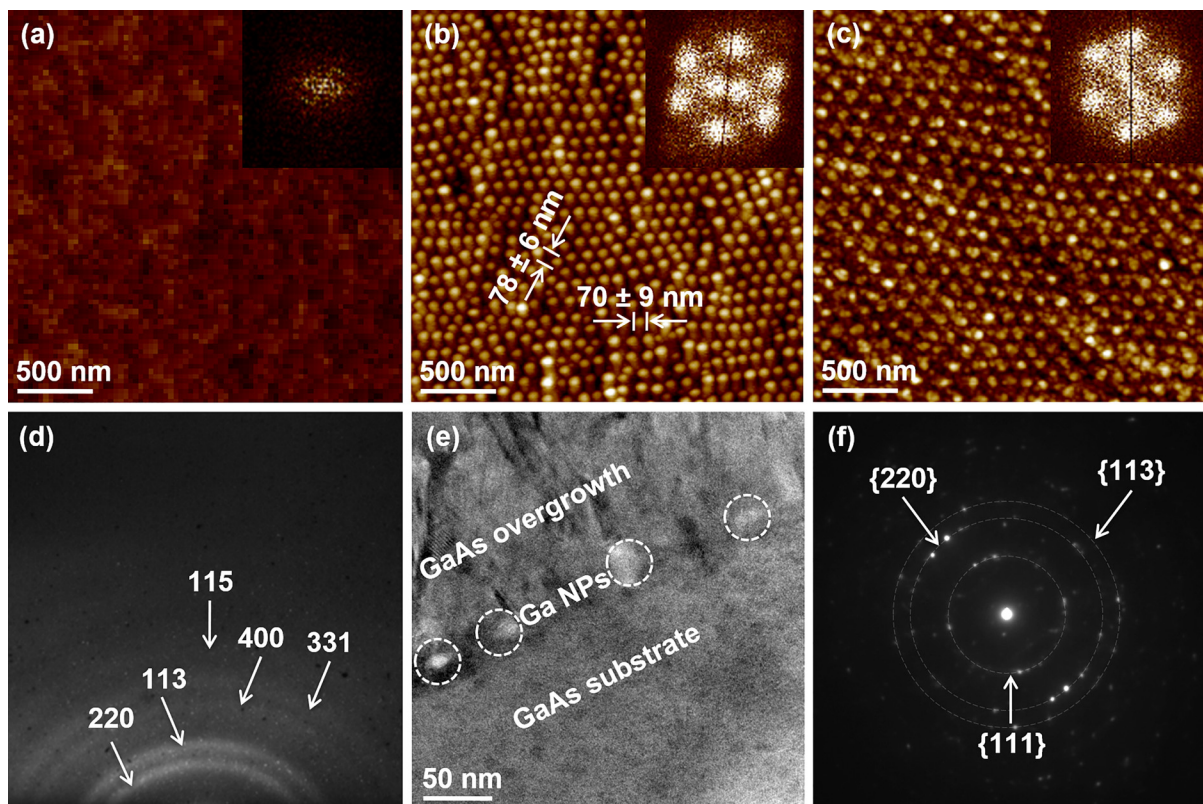


**FIG. 11.** (a)–(c) Atomic-force microscopy (AFM) images of surfaces at each step of the focused-ion-beam (FIB) patterning and molecular-beam epitaxy (MBE) overgrowth process, with total color-scale ranges displayed (a)  $\Delta z = 3.1 \text{ nm}$ , (b)  $\Delta z = 10 \text{ nm}$ , and (c)  $\Delta z = 23 \text{ nm}$ ; (a) featureless GaAs surface, without Ga nanoparticles (NPs), with corresponding featureless FFT shown as inset. (b) NP arrays (average NP diameter of 40 nm), prior to MBE overgrowth, with FFT consistent with the elongated hexagonal arrays of NPs. (c) NP arrays following 50 nm GaAs overgrowth, with similar FFT shown as inset. (d) *In situ* RHEED pattern collected immediately following 50 nm GaAs overgrowth, revealing spotty rings corresponding to multiple planes of zinc blende GaAs. (e) Cross-sectional bright-field transmission electron microscope image and (f) corresponding selected-area electron diffraction (SAED) pattern, showing amorphous Ga NP array embedded between the GaAs substrate and the MBE-overgrown GaAs layer. The SAED pattern, collected in the overgrown GaAs layer, exhibits spotty rings corresponding to multiple planes of zinc blende GaAs, consistent with the RHEED pattern in (d). Figures 11(a)–11(f) reproduced with permission from J. Appl. Phys. **122**, 033102 (2017). Copyright 2017 AIP Publishing.

and *ex situ* cross-sectional TEM images were collected. Figure 11(d) shows a RHEED pattern collected following overgrowth where spotty, concentric rings correspond to {200}, {113}, {400}, {331}, and {115} planes of zinc blende GaAs are observed.<sup>55</sup> In Fig. 11(e), a bright-field cross-sectional TEM image of overgrown Ga NP arrays (with average NP diameter of  $40 \pm 6$  nm) reveals NP arrays at the interface between the GaAs substrate and the MBE-overgrown GaAs layer.<sup>55</sup> The corresponding selected-area electron diffraction pattern shown in Fig. 11(f) exhibits spotty rings which correspond to the {111}, {200}, and {113} planes of zinc blende GaAs, consistent with the RHEED patterns discussed above.<sup>55</sup> These results demonstrate the seamless overgrowth of high-quality epitaxial polycrystalline GaAs on GaAs substrates with buried Ga NPs. Further work is needed to investigate the texture and grain size of the overgrown layer.<sup>56</sup>

## V. OPTICAL PROPERTIES OF PLASMONIC NANOCOMPOSITES

In this section, we present the plasmonic properties of both surface and buried NP arrays fabricated by the beyond threshold FIB irradiation and MBE methods described in this paper. First, we describe the surface plasmon resonances of FIB-induced Ga NP arrays on GaN surfaces. We then discuss the influences of both surface and buried Ga NP arrays on the absorption and photoluminescence efficiency of GaAs. Using a combination of PL spectroscopy and electromagnetic (EM) computations of light-matter interactions, we identify a regime of Ga NP diameter and overgrown GaAs layer thickness where NP-array-enhanced absorption in GaAs leads to enhanced GaAs near-band edge PL efficiency. These findings suggest the feasibility of utilizing a new plasmonic material (Ga) and a novel fabrication approach (FIB) for plasmonic devices. Finally, we discuss the remaining issues and opportunities for Ga NP-based plasmonics.

### A. Surface plasmon resonances of Ga NP arrays

Localized surface plasmon resonances (LSPRs) are collective oscillations of electrons induced by the interaction of radiation with subwavelength conductive layers, such as NPs.<sup>57–59</sup> For incident radiation whose frequency matches the natural frequency of electrons oscillating against the restoring force of positive nuclei, a plasmon resonance occurs. Due to their high free electron density, metals and highly doped semiconductors/oxides are typically used to induce LSPRs.<sup>57–59</sup> On semiconductor surfaces, arrays of metallic NPs have shown significant promise for a wide variety of applications including photocatalysts to boost chemical reactions,<sup>60–64</sup> optical antennas to enhance incoming signals,<sup>60,65,66</sup> surface enhanced Raman spectroscopy (SERS) to better detect analyte molecules,<sup>60,67,68</sup> and plasmonic heaters to enable photothermal/photoacoustic imaging.<sup>69,70</sup> For photocatalysts, LSPR of plasmonic NPs generated by incident radiation generates hot electrons and increases the local electric field within the surrounding medium, both of which can influence the charge of adsorbates, enhancing the catalytic reaction at the medium-adsorbate interface.<sup>60–64</sup> Since plasmonic NPs typically have high optical cross section at their resonant wavelength, they become optical antennas.<sup>60,65,66</sup> When these plasmonic NPs are located near a catalytic medium, the NPs and the nearby medium form an antenna-reactor pair where the NPs enhance the local electric field and the resulting catalytic activity of the medium.

Furthermore, many biomolecules, such as proteins and deoxyribonucleic acid (DNA), possess electronic transitions in the UV region. Specifically, illumination of metallic NPs leads to the generation of LSPRs which enhance Raman scattering from the analyte molecules. Thus, metallic NPs are useful for analyte detection via surface-enhanced Raman scattering.<sup>60,67,68</sup>

Finally, optical loss-induced heating, which has been traditionally considered a nuisance in the field of plasmonics, provides new opportunities such as photothermal and photoacoustic imaging.<sup>69,70</sup> Specifically, the thermally-induced local variation of refractive index of a medium enables a new optical microscopy technique which can detect metallic NPs with diameters below 10 nm. Also, the local temperature increase often induces the volume expansion of a surrounding medium which in turn generates an acoustic wave which can subsequently be detected.

To date, plasmonics research has focused nearly exclusively on Ag and Au NPs.<sup>57,60–73</sup> Although ensembles of Ag and Au NPs are widely produced in standard wet chemistry and device processing laboratories, they are limited by low LSPR energies (<3.5 eV) and suffer from air corrosion-induced LSPR damping.<sup>73</sup> Thus, new plasmonic materials and new fabrication methods are needed. For example, arrays of various metal NPs, including Ga, Ag, Au, In, and Ni with sizes ranging from 20 to 300 nm, have been used to access the ultraviolet, visible, and infrared LSPR energy ranges, as shown in Fig. 12. For these reports, a variety of methods, including spectroscopic ellipsometry (Ga),<sup>74–78</sup> surface-enhanced Raman scattering (Ga, In),<sup>79,80</sup> UV-Vis absorption (Ag, Au),<sup>81,82</sup> dark-field scattering (Au),<sup>83,84</sup> and far-field extinction (Ni),<sup>85</sup> were utilized to determine the LSPR energies of the NPs. Recently, using Ga NP arrays, LSPR energies in the range 0.8–5.8 eV were reported for arrays with NP diameters ranging from 10 to 300 nm.<sup>29,31,55,74–79</sup> Furthermore, a comparison of literature reports for the optical constants of liquid (amorphous) Ga and Ag NPs reveals conductivity values which are of the same order of magnitude, presumably leading to low dissipation losses in both cases.<sup>77,79</sup> Thus, both the wide tunability of LSPR energy and the low dissipation losses for Ga NPs are very promising for plasmonics. Therefore, we discuss the recent progress in understanding the optical properties of FIB-fabricated NPs and their potential for metal-semiconductor plasmonic crystals.

### B. Ga NP plasmon-enhanced GaAs photoluminescence

To facilitate understanding of the influences of surface and buried NP arrays on the photoluminescence efficiency of the GaAs gain media, we compute the absorption and spontaneous emission (SE) rate enhancement ratios of GaAs:Ga nanocomposites, in comparison to those of GaAs (Fig. 13). For this purpose, we use the finite-difference time-domain (FDTD) method to solve Maxwell's equations on a discrete spatial and temporal grid,<sup>86</sup> using perfectly matched layer boundary conditions, which allow attenuation without reflection at the boundary of the simulated space. For our simulations, a broadband plane wave is incident on a volume of vacuum layer and a nanocomposite, consisting of a square array of Ga NPs with a wide range of NP diameters, interparticle spacings, and NP depths. Using low temperature frequency-dependent complex permittivities of Ga<sup>78</sup> and GaAs<sup>87,88</sup> from the literature, the electric field,  $E(x,y,z,\omega)$ , and the absorbed (injected) optical power per unit volume  $P_{abs(injected)}(\omega) = \frac{1}{2}\omega \text{Im}(n(x,y,z,\omega))E(x,y,z,\omega)^2$  are calculated. To

determine the total absorbed (injected) optical power,  $W_{\text{abs(injected)}}$ , the absorbed (injected) optical power per unit volume is then integrated over the entire simulated space as follows:

$$W_{\text{abs(injected)}} = \int P_{\text{abs(injected)}}(\omega) dV \\ = \frac{1}{2} \omega \int \text{Im}(n(x, y, z, \omega)) E(x, y, z, \omega)^2 dV. \quad (14)$$

Subsequently, the absorptance,  $\alpha$ , is defined as the ratio of the total absorbed optical power to the total injected power as follows:

$$\alpha_{\text{NP}} = \frac{\int P_{\text{abs, NP}}(\omega) dV}{\int P_{\text{injected}}(\omega) dV}, \quad \alpha_{\text{GaAs}} = \frac{\int P_{\text{abs, GaAs}}(\omega) dV}{\int P_{\text{injected}}(\omega) dV}. \quad (15)$$

The absorption enhancement ratio is then calculated according to the following equation:

$$\text{Absorption enhancement ratio} = \frac{\alpha_{\text{NP}}}{\alpha_{\text{GaAs}}} = \frac{\int P_{\text{abs, NP}}(\omega) dV}{\int P_{\text{abs, GaAs}}(\omega) dV}. \quad (16)$$

To compute the SE rate of GaAs with surface or buried Ga NP arrays, we consider Ga NP size- and depth-dependent LSPR energies extracted from the FDTD simulation and effective dielectric permittivities based on Maxwell-Garnett effective medium approximations.<sup>89–92</sup>

To quantify the Ga NP LSPR energies at each depth, the energy-dependence of the GaAs absorption efficiency is fit to a Lorentzian function, and the maximum likelihood absorption is attributed to the LSPR energy. For each NP size and array depth, we then calculate the SE rate enhancement ratio, as follows:

SE rate enhancement ratio

$$= F \left( \frac{E(r)\mu}{|E_{\text{max}}||\mu|} \right)^2 \left( \frac{1}{1 + 4Q^2 \left( \frac{\lambda_{\text{incident}}}{\lambda} - 1 \right)^2} \right), \quad (17)$$

where  $F$  is the Purcell factor, as follows:

$$F = \frac{3}{4\pi^2} \frac{\lambda^3}{n^3} \frac{Q}{V_{\text{mode}}}, \quad (18)$$

where  $Q$  and  $V_{\text{mode}}$  are the quality factor and mode volume of the plasmonic structure, respectively. Finally, the predicted PL emission enhancement ratio is determined by the product of the absorptance enhancement ratio and the SE rate enhancement ratio.

We now consider the potential of Ga NPs for LSPR enhancement of semiconductor gain media. In Fig. 14(a), both computed and measured LSPR energies of surface (on GaAs and GaN) and embedded (within GaAs) Ga NPs are plotted as a function of NP diameter. In all cases, the LSPR energies decrease monotonically with Ga NP diameter, consistent with earlier reports shown in Fig. 12.<sup>29,31,55</sup> It is interesting to note the substrate dependence of LSPR energies, with consistently higher LSPR energies for similarly sized Ga NPs on the wider bandgap GaN surfaces in comparison with those on GaAs surfaces, as shown in Fig. 14(a). In Fig. 14(b), the PL enhancement, estimated as the ratio of the normalized PL intensities for regions of the GaAs layer, with and

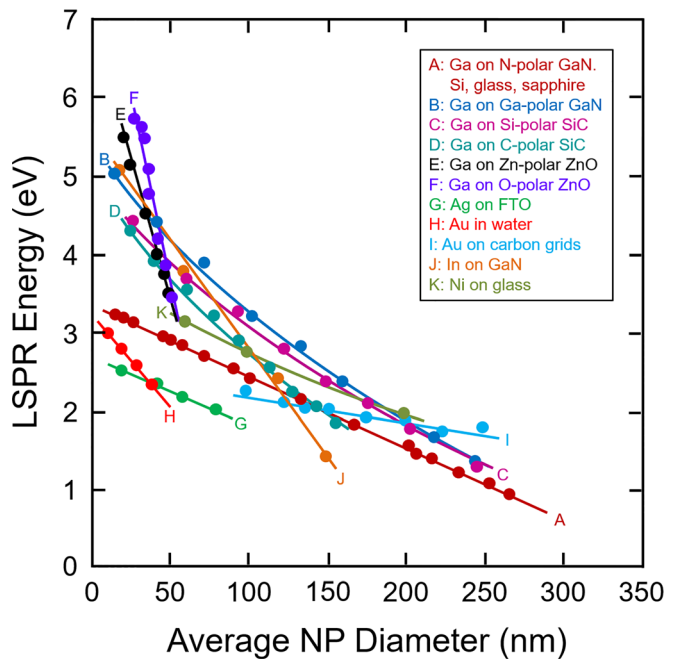


**FIG. 12.** A plot of localized-surface-plasmon resonance (LSPR) energy vs average diameter for various metallic nanoparticles (NP)s including Ga, Ag, Au, In, and Ni (A–F: Refs. 74–80, G: Ref. 81, H–I: Ref. 82–84, J: Ref. 80, and K: Ref. 85). The plot reveals that LSPR energies decrease with increasing average NP diameter. LSPR energies of Ga NPs are tunable in the range 0.8–5.8 eV.

without Ga NPs, is plotted as a function of Ga NP diameter.<sup>31,55</sup> For surface Ga NP arrays, a decrease in NP diameter from 69 to 33 nm induces an increase in the enhancement factor of GaAs PL efficiency from  $\sim 1.7$  to  $\sim 3.3$ . For embedded Ga NPs with NP depths of 40, 100, and 200 nm, a decrease in NP diameter from 66 nm to 40 nm induces increases in the enhancement factor of GaAs PL efficiency from  $\sim 1.0$  to  $\sim 1.5$ , from  $\sim 0.9$  to  $\sim 1.4$ , and from  $\sim 0.6$  to  $\sim 0.8$ , respectively. The influences of both NP diameter and overgrown GaAs thickness on the enhancement of GaAs PL efficiency allow us to identify an ideal range of the geometric parameters leading to a positive PL enhancement. Specifically, Ga NP arrays with NP diameters smaller than  $\sim 60$  nm and NP depths ranging from 0 to 100 nm enable the positive enhancement [i.e., above the horizontal dashed line in Fig. 14(b)] of GaAs PL efficiency. It is interesting to note that the maximum PL enhancements are predicted for surface and embedded Ga NP arrays with  $33.3 \pm 1.3$  nm and  $40 \pm 6$  nm diameters, respectively. Evidently, the absorption and spontaneous emission rates are influenced by both NP diameter and depth in the nanocomposite structure, producing the net PL enhancement or degradation. For both surface and buried Ga NP arrays, the GaAs PL enhancement increases monotonically with decreasing Ga NP diameter due to corresponding increases in both absorption enhancement and spontaneous emission rate enhancement.<sup>55</sup>

### C. Remaining issues and suggestions

Typically, the quality of LSPR is evaluated by its tendency as an oscillator to dampen or by its dissipation of energy within the host. To

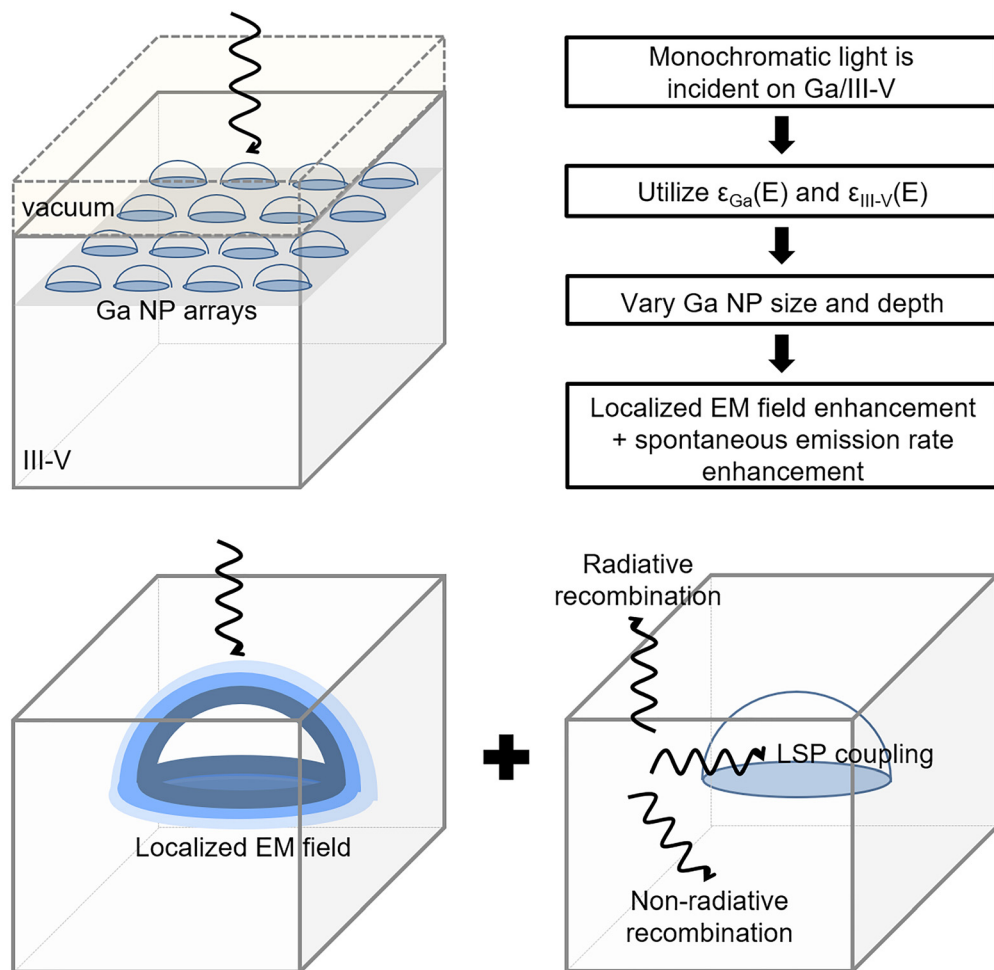


**FIG. 13.** The simulation volume is a cube of  $1 \mu\text{m}^3$  of GaAs with a 25 nm-thick vacuum layer on the top. The hemispheroidal Ga NP arrays are buried at a wide range of different depths below the GaAs surface. We use the finite-difference time-domain (FDTD) method to solve Maxwell's equations in order to quantify both the absorption enhancement induced by localized EM field due to localized-surface plasmon resonance (LSPR) of Ga NPs and spontaneous emission (SE) rate enhancements via LSPR.

quantify the bandwidth of an oscillator relative to its resonance frequency, the LSPR quality factor is defined as  $Q_{\text{LSPR}} = f_r/\Delta f$ , where  $f_r$  is the resonance frequency and  $\Delta f$  is the full width half maximum of the resonance.<sup>93</sup> For comparison, the  $Q_{\text{LSPR}}$  values for various metals with LSPRs in the visible and near-IR, including Ag, Au, and Ga NPs, are illustrated in Fig. 15(a). For Ag NPs,<sup>93</sup>  $Q_{\text{LSPR}}$  ranges from 3.83 to 7.61; for Au nanoshells,<sup>94,95</sup>  $Q_{\text{LSPR}}$  ranges from 1 to 2; and for Ga NPs,<sup>29</sup>  $Q_{\text{LSPR}}$  ranges from 1.9 to 3.5. It is interesting to note that the value of  $Q_{\text{LSPR}}$  for Ga NPs is comparable to those reported for Ag and Au NPs. Alternatively, to quantify dissipation of energy within the host, the quality factor is defined as  $Q_{\text{Loss}} = -\epsilon_{\text{real}}/\epsilon_{\text{imaginary}}$ , where  $\epsilon_{\text{real}}$  and  $\epsilon_{\text{imaginary}}$  correspond to the real and imaginary parts of the host dielectric function, respectively.<sup>96</sup> In Fig. 15(b), plots of  $Q_{\text{Loss}}$  vs wavelength are shown for Ga NPs<sup>76,97</sup> and other metals including Ag, Au, Na, K, and Al NPs.<sup>96</sup> It is interesting to note that the values of  $Q_{\text{Loss}}$  for Ag NPs are significantly larger than those of Ga and other metallic NPs. Indeed, Ag, with its large negative  $\epsilon_{\text{real}}$  and low  $\epsilon_{\text{imaginary}}$  is expected to

exhibit low losses; therefore, it has been the plasmonic material of choice.<sup>1,89–91,93</sup>

Although Ga and other metals are intrinsically lossy, the loss can be reduced or mitigated via tailoring of the nanostructure geometry. For example, it has been reported that hybrid nanostructures such as core-shell structures can effectively localize plasmon resonances.<sup>98,99</sup> Also, alternative approaches which exploit intrinsic losses have been proposed and demonstrated. For example, loss-induced heating has been used as the temperature readout during photothermal imaging.<sup>69,70,99</sup> Since our method enables the “shelling” of Ga NPs using semiconductor epitaxy, the resulting core-shell structure may provide new opportunities. Furthermore, although an inert, self-terminating native oxide layer typically formed on the surface of Ga NPs protects the core and enables long-term stability in optical properties, their low melting point of 303 K makes the shape of the corresponding nanostructures easily changed under ambient conditions which could be detrimental to plasmonic applications. We foresee that this issue can

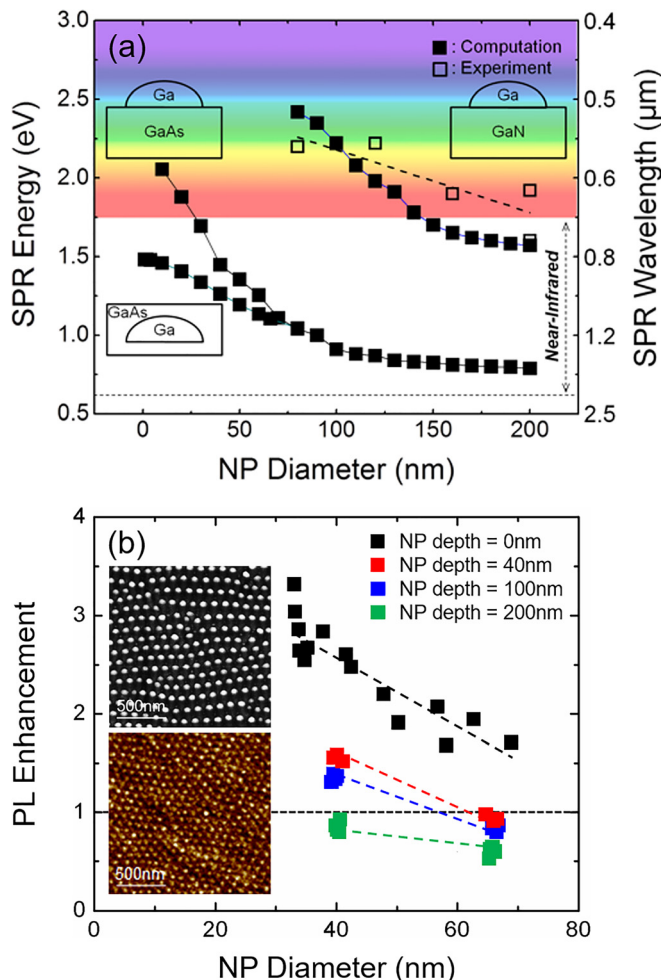


**FIG. 14.** (a) Plots of calculated and measured localized surface plasmon resonance (LSPR) energy vs average diameter of Ga NP. The calculations assume that a Ga NP is either in GaAs or on GaAs and GaN. The plot reveals that Ga LSPR energies range from 0.8 to 2.5 eV, showing a decreasing trend with an increasing diameter of NPs. (b) Measured PL enhancements as a function of Ga NP diameter for Ga NPs on GaAs surfaces and Ga NPs embedded in GaAs layers. In (a) and (b), each data point is based upon measurements of five different regions; the error bars, which are determined by counting statistics, are smaller than the size of symbols. Figures 14(a) and 14(b) reproduced with permission from Appl. Phys. Lett. **101**, 081905 (2012). Copyright 2012 AIP Publishing; Appl. Phys. Lett. **103**, 101903 (2013). Copyright 2013 AIP Publishing; and J. Appl. Phys. **122**, 033102 (2017). Copyright 2017 AIP Publishing.

be mitigated by alloying Ga with other plasmonic materials, thereby enabling their widespread use in practical applications.

## VI. SUMMARY

In summary, in this review article, we described the recent progress in the FIB irradiation-directed self-assembly of surface and embedded metallic nanostructure arrays. Following a description of semiquantitative calculations of sputtering yields, surface nonstoichiometry, and the resulting threshold ion doses for group III segregation, we discussed the relationship between sputtering

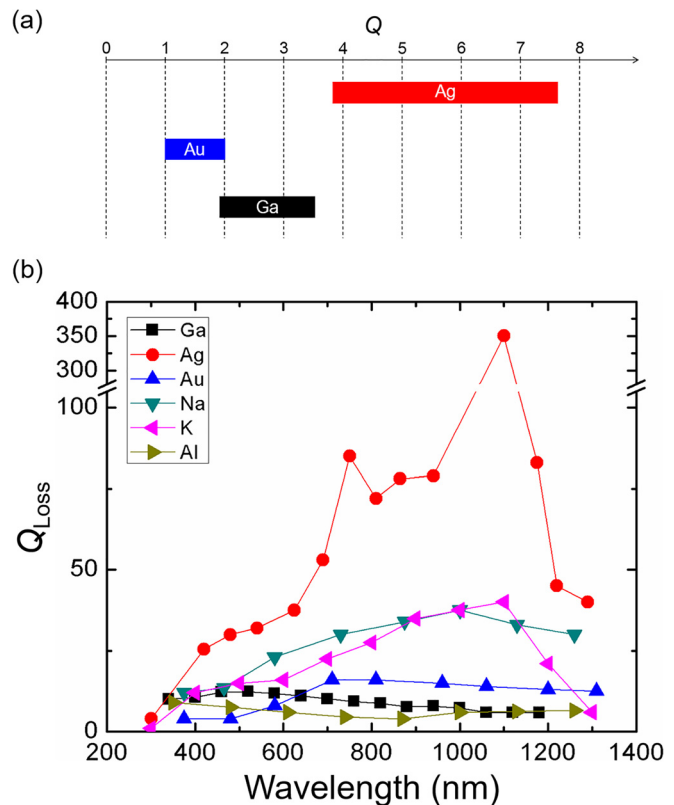


**FIG. 15.** (a) A diagram showing the measured values of the localized-surface-plasmon resonance quality factor,  $Q_{\text{LSPR}}$ , reported for Ag, Au, and Ga NPs. It is interesting to note that the value of  $Q_{\text{LSPR}}$  for Ga NPs is comparable to those reported for Ag and Au NPs. (b) Plots of measured quality factors,  $Q_{\text{Loss}} = -\epsilon_{\text{real}}/\epsilon_{\text{imaginary}}$ , where  $\epsilon_{\text{real}}$  and  $\epsilon_{\text{imaginary}}$  are the real and imaginary dielectric functions of the host, for Ga NPs and other metals including Ag, Au, Na, K, and Al NPs. Figure 15(b) reproduced with permission from West *et al.*, Laser Photonics. Rev. **4**, 795 (2010). Copyright 2010 WILEY-VCH.

yield trends and nanostructure array types. For Ga-V substrates with high, moderate, and low sputtering yields, vertical arrays (GaSb: GaSb NRs with Ga tips), NP arrays (GaAs: Ga NPs), and lateral NC arrays (GaN: Ga NCs) are observed. The sputtering yield-nanostructure type relationship is expected to be applicable to a wide variety of III-V and II-VI compound semiconductor surfaces. Next, we described the formation of close-packed embedded Ga:GaAs nanocomposites using MBE overgrowth of FIB-fabricated NP arrays. Finally, we presented the plasmonic properties of Ga NP arrays and discussed the influence of both surface and buried NP arrays on the optical properties of semiconductor gain media.

## ACKNOWLEDGMENTS

This research was supported by the National Science Foundation through the Materials Research Science and Engineering Center at the University of Michigan, Grant No. DMR-1120923, and by the Defense University Research Instrumentation Program through the Army Research Office,

Grant No. W911NF-07-1-0344. We thank S. Jeon, A. A. Al-Heji, J.-E. Lee, T. W. Saucer, V. Sih, and D. S. Schulman for useful discussions.

## REFERENCES

- <sup>1</sup>T. Huang, W. Cao, H. E. Elsayed-Ali, and X. N. Xu, "High-throughput ultra-sensitive characterization of chemical, structural and plasmonic properties of EBL-fabricated single silver nanoparticles," *Nanoscale* **4**, 380 (2012).
- <sup>2</sup>A. L. Giermann and C. V. Thompson, "Solid-state dewetting for ordered arrays of crystallographically oriented metal particles," *Appl. Phys. Lett.* **86**, 121903 (2005).
- <sup>3</sup>J. Lian, L. Wang, X. Sun, Q. Yu, and R. C. Ewing, "Patterning metallic nanostructures by ion-beam-induced dewetting and rayleigh instability," *Nano Lett.* **6**, 1047 (2006).
- <sup>4</sup>P. D. Rack, Y. Guan, J. D. Fowlkes, A. V. Melechko, and M. L. Simpson, "Pulsed laser dewetting of patterned thin metal films: A means of directed assembly," *Appl. Phys. Lett.* **92**, 223108 (2008).
- <sup>5</sup>Y. Oh, C. A. Ross, Y. S. Jung, Y. Wang, and C. V. Thompson, "Cobalt nanoparticle arrays made by templated solid-state dewetting," *Small* **5**, 860 (2009).
- <sup>6</sup>Y. Wu, J. D. Fowlkes, P. D. Rack, J. A. Diez, and L. Kondic, "On the breakup of patterned nanoscale copper rings into droplets via pulsed-laser-induced dewetting: Competing liquid-phase instability and transport mechanisms," *Langmuir* **26**, 11972 (2010).
- <sup>7</sup>J. Ye and C. V. Thompson, "Templated solid-state dewetting to controllably produce complex patterns," *Adv. Mater.* **23**, 1567 (2011).
- <sup>8</sup>F. Ruffinosa and M. G. Grimaldi, "Template-confined dewetting of Au and Ag nanoscale films on mica substrate," *Appl. Surf. Sci.* **270**, 697 (2013).
- <sup>9</sup>M. Kang, Y. Yuwen, W. Hu, S. Yun, K. Mahalingam, B. Jiang, K. Eyink, E. Poutrina, K. Richardson, and T. S. Mayer, "Self-organized freestanding one-dimensional au nanoparticle arrays," *ACS Nano* **11**, 5844 (2017).
- <sup>10</sup>A. Kumar, S. Mandal, S. P. Mathew, P. R. Selvakannan, A. B. Mandale, R. V. Chaudhari, and M. Sastry, "Benzene- and anthracene-mediated assembly of gold nanoparticles at the liquid-liquid interface," *Langmuir* **18**, 6478 (2002).
- <sup>11</sup>L. S. Slaughter, L. Wang, B. A. Willingham, J. M. Olson, P. Swanglap, S. Dominguez-Medinaab, and S. Link, "Plasmonic polymers unraveled through single particle spectroscopy," *Nanoscale* **6**, 11451 (2014).
- <sup>12</sup>M. Yang, G. Chen, Y. Zhao, G. Silber, Y. Wang, S. Xing, Y. Han, and H. Chen, "Mechanistic investigation into the spontaneous linear assembly of gold nanospheres," *Phys. Chem. Chem. Phys.* **12**, 11850 (2010).
- <sup>13</sup>S. Facsko, T. Dekorsy, C. Koerdt, C. Trappe, H. Kurz, A. Vogt, and H. L. Hartnagel, "Formation of ordered nanoscale semiconductor dots by ion sputtering," *Science* **285**, 1551 (1999).
- <sup>14</sup>B. R. Jany, K. Szajna, M. Nikiel, D. Wrana, E. Trynkiewicz, R. Pedrys, and F. Krok, "Energy dependence of nanopillars formation on InSb semiconductor surfaces under gallium FIB and noble gas ions beam irradiation," *Appl. Surf. Sci.* **327**, 86 (2015).
- <sup>15</sup>J. H. Wu and R. S. Goldman, "Mechanisms of nanorod growth on focused-ion-beam-irradiated semiconductor surfaces: Role of redeposition," *Appl. Phys. Lett.* **100**, 053103 (2012).
- <sup>16</sup>M. Kang, J. H. Wu, W. Ye, Y. Jiang, E. A. Robb, C. Chen, and R. S. Goldman, "Formation and evolution of ripples on ion-irradiated semiconductor surfaces," *Appl. Phys. Lett.* **104**, 052103 (2014).
- <sup>17</sup>M. Tanemura, S. Aoyama, Y. Fujimoto, and F. Okuyama, "Structural and compositional analyses of cones formed on ion-sputtered GaAs surfaces," *Nucl. Instrum. Methods Phys. Res. B* **61**, 451 (1991).
- <sup>18</sup>M. Bouslama, C. Jardin, and M. Ghannina, "The InSb(100) surface change during the argon ion bombardment and the electron stimulated oxidation," *Vacuum* **46**, 143 (1995).
- <sup>19</sup>M. Tanemura, T. Aoyama, A. Otani, M. Ukita, F. Okuyama, and T. K. Chini, "Angular distribution of In and P particles sputtered from InP by inert-gas ion bombardment," *Surf. Sci.* **376**, 163 (1997).
- <sup>20</sup>A. Lugstein, M. Weil, B. Basnar, C. Tomastik, and E. Bertagnoli, "A novel fabrication technique for crystalline growth on a (100) InAs surface utilizing focused ion beams," *Nucl. Instrum. Methods Phys. Res. B* **222**, 91 (2004).
- <sup>21</sup>S. K. Tan and A. T. S. Wee, "Self-organized nanodot formation on InP(100) by argon ion sputtering at normal incidence," *J. Vac. Sci. Technol. B* **24**, 1444 (2006).
- <sup>22</sup>J. L. Plaza and E. Dieguez, "Influence of Au diffusion on the formation of nanodot hexagonal ordered arrays on GaSb substrates by low energy ion sputtering," *Solid State Ionics* **178**, 1576 (2007).
- <sup>23</sup>F. Krok, "Study of the chemical and morphological evolution in InSb(001) surface under low energy ion bombardment," *Vacuum* **83**, 745 (2008).
- <sup>24</sup>Q. Wei, J. Lian, W. Lu, and L. Wang, "Highly ordered Ga nanodroplets on a GaAs surface formed by a focused ion beam," *Phys. Rev. Lett.* **100**, 076103 (2008).
- <sup>25</sup>J. H. Wu, W. Ye, B. L. Cardozo, D. Saltzman, K. Sun, H. Sun, J. F. Mansfield, and R. S. Goldman, "Formation and coarsening of Ga droplets on focused-ion-beam irradiated GaAs surfaces," *Appl. Phys. Lett.* **95**, 153107 (2009).
- <sup>26</sup>E. Despiau-Pujo and P. Chabert, "MD simulations of GaN sputtering by Ar<sup>+</sup> ions: Ion-induced damage and near-surface modification under continuous bombardment," *J. Vac. Sci. Technol. A* **28**, 1105 (2010).
- <sup>27</sup>K. A. Grossklaus and J. M. Millunchick, "Mechanisms of nanodot formation under focused ion beam irradiation in compound semiconductors," *J. Appl. Phys.* **109**, 014319 (2011).
- <sup>28</sup>M. Kang, J. H. Wu, S. Huang, M. V. Warren, Y. Jiang, E. A. Robb, and R. S. Goldman, "Universal mechanism for ion-induced nanostructure formation on III-V compound semiconductor surfaces," *Appl. Phys. Lett.* **101**, 082101 (2012).
- <sup>29</sup>M. Kang, T. W. Saucer, M. V. Warren, J. H. Wu, V. Sih, and R. S. Goldman, "Surface plasmon resonances of Ga nanoparticle arrays," *Appl. Phys. Lett.* **101**, 081905 (2012).
- <sup>30</sup>S. Lee, L. Wang, and W. Lu, "Formation of ordered nanodroplet chains on a solid surface by enhanced surface diffusion and shadow effect," *Surf. Sci.* **606**, 659 (2012).
- <sup>31</sup>M. Kang, A. A. Al-Heji, J.-E. Lee, T. W. Saucer, S. Jeon, J. H. Wu, L. Zhao, A. L. Katzenstein, D. L. Sofferman, V. Sih, and R. S. Goldman, "Ga nanoparticle-enhanced photoluminescence of GaAs," *Appl. Phys. Lett.* **103**, 101903 (2013).
- <sup>32</sup>M. Kang, J. H. Wu, D. L. Sofferman, I. Beskin, H. Y. Chen, K. Thornton, and R. S. Goldman, "Origins of ion irradiation-induced Ga nanoparticle motion on GaAs surfaces," *Appl. Phys. Lett.* **103**, 072115 (2013).
- <sup>33</sup>M. Kang, I. Beskin, A. A. Al-Heji, O. Shende, S. Huang, S. Jeon, and R. S. Goldman, "Evolution of ion-induced nanoparticle arrays on GaAs surfaces," *Appl. Phys. Lett.* **104**, 182102 (2014).
- <sup>34</sup>S. W. Maclarens, J. E. Baker, N. L. Finnegan, and C. M. Loxton, "Surface roughness development during sputtering of GaAs and InP: Evidence for the role of surface diffusion in ripple formation and sputter cone development," *J. Vac. Sci. Technol. A* **10**, 468 (1992).
- <sup>35</sup>F. Rose, H. Fujita, and H. Kawakatsu, "Real-time observation of FIB-created dots and ripples on GaAs," *Nanotechnology* **19**, 035301 (2008).
- <sup>36</sup>W. J. MoyerChan, D. P. Adams, M. J. Aziz, G. Hobler, and T. Schenkel, "Fundamentals of focused ion beam nanostructural processing: Below, at, and above the surface," *MRS Bull.* **32**, 424 (2007).
- <sup>37</sup>S. Lancaster, M. Kriz, M. Schinnerl, D. MacFarland, T. Zederbauer, A. M. Andrews, W. Schrenk, G. Strasser, and H. Detz, "Focused ion beam implantation for the nucleation of self-catalyzed III-V nanowires," *Microelectron. Eng.* **177**, 93 (2017).
- <sup>38</sup>H. Okamoto, M. E. Schlesinger, and E. M. Mueller, *ASM Handbook: Alloy Phase Diagrams Volume 3* (ASM International, Ohio, 1992).
- <sup>39</sup>J. Tesmer and M. Nastasi, *Handbook of Modern Ion Beam Materials Analysis* (Materials Research Society, Pennsylvania, 1995).
- <sup>40</sup>M. Nastasi, J. W. Mayer, and J. K. Hirvonen, *Ion-Solid Interactions: Fundamentals and Applications* (Cambridge University Press, Cambridge, 1996).
- <sup>41</sup>P. Sigmund, "Theory of sputtering. I. Sputtering yield of amorphous and polycrystalline targets," *Phys. Rev.* **184**, 383 (1969).
- <sup>42</sup>L. Liau and J. W. Mayer, "Limits of composition achievable by ion implantation," *J. Vac. Sci. Technol. B* **15**, 1629 (1978).
- <sup>43</sup>D. Santamore, K. Edinger, J. Orloff, and J. Melngailis, "Focused ion beam sputter yield change as a function of scan speed," *J. Vac. Sci. Technol. B* **15**, 2346 (1997).
- <sup>44</sup>F. X. Wang, F. Lu, H. Hu, F. Chen, J. H. Zhang, and Q. M. Lu, "The mean projected ranges, range straggling and lateral spreads of Er, Nd ions implanted in Si<sub>1</sub>N<sub>1.375</sub>H<sub>0.603</sub>," *Appl. Surf. Sci.* **195**, 48 (2002).

- <sup>45</sup>J. Orloff, M. Utlaut, and L. Swanson, *High Resolution Focused Ion Beams* (Kluwer Academic, New York, 2003).
- <sup>46</sup>R. Cuerno and M. Castro, *Toward Functional Nanomaterials* (Springer New York, New York, 2009), Vol. 5.
- <sup>47</sup>M. Castro, R. Cuerno, L. Vazquez, and R. Gago, "Self-organized ordering of nanostructures produced by ion-beam sputtering," *Phys. Rev. Lett.* **94**, 016102 (2005).
- <sup>48</sup>F. Frost, B. Ziberi, T. Hoche, and B. Rauschenbach, "The shape and ordering of self-organized nanostructures by ion sputtering," *Nucl. Instrum. Methods B* **216**, 9 (2004).
- <sup>49</sup>F. Frost, B. Ziberi, A. Schindler, and B. Rauschenbach, "Surface engineering with ion beams: From self-organized nanostructures to ultra-smooth surfaces," *Appl. Phys. A* **91**, 551 (2008).
- <sup>50</sup>S. Y. Chou, P. R. Krauss, W. Zhang, L. J. Guo, and L. Zhuang, "Sub-10 nm imprint lithography and applications," *J. Vac. Sci. Technol. B* **15**, 2897 (1997).
- <sup>51</sup>S. Y. Chou, P. R. Krauss, and P. J. Renstrom, "Imprint lithography with 25-nanometer resolution," *Science* **272**, 85 (1996).
- <sup>52</sup>M. Park, C. Harrison, P. M. Chaikin, R. A. Register, and D. H. Adamson, "Block copolymer lithography: Periodic arrays of  $\sim 10^{11}$  holes in 1 square centimeter," *Science* **276**, 1401 (1997).
- <sup>53</sup>Y. N. Xia and G. M. Whitesides, "Soft lithography," *Annu. Rev. Mater. Sci.* **28**, 153 (1998).
- <sup>54</sup>H. Holland-Moritz, A. Ilinov, F. Djurabekova, K. Nordlund, and C. Ronning, "Sputtering and redeposition of ion irradiated Au nanoparticle arrays: Direct comparison of simulations to experiments," *New J. Phys.* **19**, 013023 (2017).
- <sup>55</sup>M. Kang, S. Jeon, T. Jen, J.-E. Lee, V. Sih, and R. S. Goldman, "Formation of embedded plasmonic Ga nanoparticle arrays and their influence on GaAs photoluminescence," *J. Appl. Phys.* **122**, 033102 (2017).
- <sup>56</sup>S. Jeon, "Gallium metal nanoparticles for plasmonics and droplet epitaxy: Formation and properties," Ph.D. thesis (University of Michigan, 2016).
- <sup>57</sup>K. A. Willets and R. P. Van Duyne, "Localized surface plasmon resonances spectroscopy and sensing," *Annu. Rev. Phys. Chem.* **58**, 267 (2007).
- <sup>58</sup>K. Manthiram and A. P. Alivisatos, "Tunable localized surface plasmon resonances in tungsten oxide nanocrystals," *J. Am. Chem. Soc.* **134**, 3995 (2012).
- <sup>59</sup>J. A. Faucheaux, A. L. D. Stanton, and P. K. Jain, "Plasmon resonances of semiconductor nanocrystals: Physical principles and new opportunities," *J. Phys. Chem. Lett.* **5**, 976 (2014).
- <sup>60</sup>S. Kim, J.-M. Kim, J.-E. Park, and J.-M. Nam, "Nonnoble-metal-based plasmonic nanomaterials: Recent advances and future perspectives," *Adv. Mater.* **30**, 1704528 (2018).
- <sup>61</sup>W. Hou and S. B. Cronin, "A review of surface plasmon resonance-enhanced photocatalysis," *Adv. Funct. Mater.* **23**, 1612 (2013).
- <sup>62</sup>S. Peng, M. T. Sheldon, W.-G. Liu, A. Jaramillo-Botero, W. A. Goddard III, and H. A. Atwater, "Ultraviolet surface plasmon-mediated low temperature hydrazine decomposition," *Appl. Phys. Lett.* **106**, 023102 (2015).
- <sup>63</sup>G. Dodekatos, S. Schunemann, and H. Tuysuz, "Surface plasmon-assisted solar energy conversion," *Top. Curr. Chem.* **371**, 215 (2015).
- <sup>64</sup>H. Wang, L. Cui, S. Chen, M. Guo, S. Lu, and Y. Xiang, "A new perspective on metal particles enhanced MoS<sub>2</sub> photocatalysis in hydrogen evolution: Excited electric field by surface plasmon resonance," *J. Appl. Phys.* **126**, 015101 (2019).
- <sup>65</sup>M. B. Ross and G. C. Schatz, "Aluminum and indium-plasmonic nanoantennas in the ultraviolet," *J. Phys. Chem. C* **118**, 12506 (2014).
- <sup>66</sup>D. F. Sweare, H. Zhao, L. Zhou, C. Zhang, H. Robatjazi, J. M. P. Martirez, C. M. Krauter, S. Yazdi, M. J. McClain, E. Ringe, E. A. Carter, P. Nordlander, and N. J. Halas, "Heterometallic antenna-reactor complexes for photocatalysis," *Proc. Natl. Acad. Sci. U. S. A.* **113**, 8916 (2016).
- <sup>67</sup>S. Schlucker, "Surface-enhanced Raman spectroscopy: Concepts and chemical applications," *Angew. Chem., Int. Ed.* **53**, 4756 (2014).
- <sup>68</sup>B. Cerjan, X. Yang, P. Nordlander, and N. J. Halas, "Asymmetric aluminum antennas for self-calibrating surface-enhanced infrared absorption spectroscopy," *ACS Photonics* **3**, 354 (2016).
- <sup>69</sup>G. Baffou and R. Quidant, "Thermo-plasmonics: Using metallic nanostructures as nano-sources of heat," *Laser Photonics Rev.* **7**, 171 (2013).
- <sup>70</sup>D. J. de Aberasturi, A. B. Serrano-Montes, and L. M. Liz-Marzan, "Modern applications of plasmonic nanoparticles: From energy to health," *Adv. Opt. Mater.* **3**, 602 (2015).
- <sup>71</sup>B. N. Khlebtsov and N. G. Khlebtsov, "Multipole plasmons in metal nanorods: Scaling properties and dependence on particle size, shape, orientation, and dielectric environment," *J. Phys. Chem. C* **111**, 11516 (2007).
- <sup>72</sup>A. Liebsch, "Surface-plasmon dispersion and size dependence of Mie resonance: Silver versus simple metals," *Phys. Rev. B* **48**, 11317 (1993).
- <sup>73</sup>A. Yelon, K. N. Piyakis, and E. Sacher, "Surface plasmon in Drude metals," *Surf. Sci.* **569**, 47 (2004).
- <sup>74</sup>P. C. Wu, M. Losurdo, T.-H. Kim, S. Choi, G. Bruno, and A. S. Brown, "In situ spectroscopic ellipsometry to monitor surface plasmon resonant group-III metals deposited by molecular beam epitaxy," *J. Vac. Sci. Technol. B* **25**, 1019 (2007).
- <sup>75</sup>P. C. Wu, T.-H. Kim, A. S. Brown, M. Losurdo, G. Brown, and H. O. Everitt, "Real-time plasmon resonance tuning of liquid Ga nanoparticles by in situ spectroscopic ellipsometry," *Appl. Phys. Lett.* **90**, 103119 (2007).
- <sup>76</sup>P. C. Wu, M. Losurdo, T.-H. Kim, M. Giangregorio, G. Bruno, H. O. Everitt, and A. S. Brown, "Plasmonic gallium nanoparticles on polar semiconductors: Interplay between nanoparticle wetting, localized surface plasmon dynamics, and interface charge," *Langmuir* **25**, 924 (2009).
- <sup>77</sup>Y. Yang, N. Akozbek, T.-H. Kim, J. M. Sanz, F. Moreno, M. Losurdo, and A. S. Brown, "Ultraviolet-visible plasmonic properties of gallium nanoparticles investigated by variable-angle spectroscopic and Mueller matrix ellipsometry," *ACS Photonics* **1**, 582 (2014).
- <sup>78</sup>M. W. Knight, T. Coenen, Y. Yang, B. J. M. Brenny, M. Losurdo, A. S. Brown, H. O. Everitt, and A. Polman, "Gallium plasmonics: Deep subwavelength spectroscopic imaging of single and interacting gallium nanoparticles," *ACS Nano* **9**, 2049 (2015).
- <sup>79</sup>P. C. Wu, C. G. Khoury, T.-H. Kim, Y. Yang, M. Losurdo, G. V. Bianco, T. Vo-Dinh, A. S. Brown, and H. O. Everitt, "Demonstration of surface-enhanced Raman scattering by tunable, plasmonic gallium nanoparticles," *J. Am. Chem. Soc.* **131**, 12032 (2009).
- <sup>80</sup>P. Wu, "Plasmon gallium nanoparticles—Attributes and applications," Ph.D. dissertation (Duke University, 2009).
- <sup>81</sup>K.-C. Lee, S.-J. Lin, C.-H. Lin, C.-S. Tsai, and Y.-J. Lu, "Size effect of Ag nanoparticles on surface plasmon resonance," *Surf. Coat. Technol.* **202**, 5339 (2008).
- <sup>82</sup>W. Haiss, N. T. K. Thanh, J. Aveyard, and D. G. Fernig, "Determination of size and concentration of gold nanoparticles from UV-Vis spectra," *Anal. Chem.* **79**, 4215 (2007).
- <sup>83</sup>C. Sonnichsen, T. Franzl, T. Wilk, G. Von Plessen, and J. Feldmann, "Plasmon resonances in large noble-metal clusters," *New J. Phys.* **4**, 93 (2002).
- <sup>84</sup>E. Ringe, M. R. Langille, K. Sohn, J. Zhang, J. Huang, C. A. Mirkin, R. P. Van Duyne, and L. D. Marks, "Plasmon length: A universal parameter to describe size effects in gold nanoparticles," *J. Phys. Chem. Lett.* **3**, 1479 (2012).
- <sup>85</sup>J. Chen, P. Albella, Z. Pirzadeh, P. Alonso-Gonzalez, F. Huth, S. Bonetti, V. Bonanni, J. Akerman, J. Nogues, P. Vavassori, A. Dmitriev, J. Aizpurua, and R. Hillenbrand, "Plasmonic nickel nanoantennas," *Small* **7**, 2341 (2011).
- <sup>86</sup>See [https://kb.lumerical.com/solvers\\_finite\\_difference\\_time\\_domain.html](https://kb.lumerical.com/solvers_finite_difference_time_domain.html).
- <sup>87</sup>M. Scalora, M. A. Vincenti, V. Roppo, J. V. Foreman, J. W. Haus, N. Akozbek, and M. J. Bloemer, "New propagation effects in semiconductors in the UV range: Inhibition of absorption, negative refraction, anomalous momentum states, sub-wavelength imaging, and non-plasmonic nanometer-size guided waves," in IEEE/LEOS Conference (2009), p. 132.
- <sup>88</sup>I. Strzalkowski, S. Joshi, and C. R. Crowell, "Dielectric constant and its temperature dependence for GaAs, CdTe, and ZnSe," *Appl. Phys. Lett.* **28**, 350 (1976).
- <sup>89</sup>P. Spinelli and A. Polman, "Prospects of near-field plasmonic absorption enhancement in semiconductor materials using embedded Ag nanoparticles," *Opt. Express* **20**, A641 (2012).
- <sup>90</sup>G. Xu, M. Tazawa, P. Jin, S. Nakao, and K. Yoshimura, "Wavelength tuning of surface plasmon resonance using dielectric layers on silver island films," *Appl. Phys. Lett.* **82**, 3811 (2003).
- <sup>91</sup>X. Liu, D. Li, X. Sun, Z. Li, H. Song, H. Jiang, and Y. Chen, "Tunable dipole surface plasmon resonances of silver nanoparticles by cladding dielectric layers," *Sci. Rep.* **5**, 12555 (2015).
- <sup>92</sup>D. Englund, D. Fattal, E. Waks, G. Solomon, B. Zhang, T. Nakaoka, Y. Arakawa, Y. Yamamoto, and J. Vuckovic, "Controlling the spontaneous emission rate of single quantum dots in a two-dimensional photonic crystal," *Phys. Rev. Lett.* **95**, 013904 (2005).

- <sup>93</sup>T. R. Jensen, M. D. Malinsky, C. L. Haynes, and R. P. V. Duyne, "Nanosphere lithography: Tunable localized surface plasmon resonance spectra of silver nanoparticles," *J. Phys. Chem. B* **104**, 10549 (2000).
- <sup>94</sup>S. J. Oldenburg, J. B. Jackson, S. L. Westcott, and N. J. Halas, "Infrared extinction properties of gold nanoshells," *Appl. Phys. Lett.* **75**, 2897 (1999).
- <sup>95</sup>S. J. Oldenburg, R. D. Averitt, S. L. Westcott, and N. J. Halas, "Nanoengineering of optical resonances," *Chem. Phys. Lett.* **288**, 243 (1998).
- <sup>96</sup>P. R. West, S. Ishii, G. V. Naik, N. K. Emani, V. M. Shalaev, and A. Boltasseva, "Searching for better plasmonic materials," *Laser Photonics Rev.* **4**, 795 (2010).
- <sup>97</sup>M. Kang, "Formation and properties of metallic nanoparticles on compound semiconductor surfaces," Ph.D. thesis (University of Michigan, 2014).
- <sup>98</sup>U. Kreibig and M. Vollmer, *Optical Properties of Metal Clusters* (Springer-Verlag, Berlin, 1995).
- <sup>99</sup>S. V. Boriskina, T. A. Cooper, L. Zeng, G. Ni, J. K. Tong, Y. Tsurimaki, Y. Huang, L. Meroueh, G. Mahan, and G. Chen, "Losses in plasmonics: From mitigating energy dissipation to embracing loss-enabled functionalities," *Adv. Opt. Photonics* **9**, 775 (2017).